Identification of relativistic particles from ionization in gas

G. I. Merzon

P. N. Lebedev Physics Institute, USSR Academy of Sciences, Moscow

B. Sitar

J. A. Komenský University, Bratislava

Yu. A. Budagov

Joint Institute for Nuclear Research, Dubna

Fiz. Elem. Chastits At. Yadra **14**, 648–726 (May–June 1983)

The theoretical basis and the experimental methods for identifying relativistic charged particles by measuring ionization energy loss and specific primary ionization are described. Methods for determining more accurately the probable ionization energy loss in multilayer detectors are analyzed. The construction and performance of large proportional and drift chambers used in modern physics experiments are described. The factors that influence the reliability of the identification of the particles in multilayer detectors and determine the intrinsic space and time resolution of these instruments are investigated. The possibilities and conditions of identification of particles by measurement of the specific primary ionization in streamer chambers, by cluster counting in drift chambers, and by the efficiency of a gas-discharge detector and the spark formation time in spark chambers are considered.

PACS numbers: 29.40.Jz, 29.40.Hy, 29.70.Gn

INTRODUCTION

Methods of identifying relativistic charged particles

In high-energy physics experiments it is frequently necessary to determine the nature of an investigated particle, i.e., to recognize or identify it. The identification of charged particles with energy in the range from a few giga-electron-volts to several tens of giga-electron-volts is a fairly complicated experimental problem. Whereas charged leptons (e, μ) can be recognized on the basis of the nature of their interaction in matter, all methods for identifying charged hadrons (π, K, p) are based solely on the differences between their masses.

To estimate the mass m of a singly charged relativistic particle, it is necessary to know two independent characteristics of the particle. The first of these is usually the momentum p or the energy E, which can be measured from the deflection in a magnetic field or the energy release in a total-absorption spectrometer. Another characteristic may be the velocity $v = \beta c$ of the particle, determined from the time of flight or from the angle and intensity of Cherenkov radiation, and also the Lorentz factor $\gamma = E/mc^2 = (1 - \beta^2)^{-1/2}$, which can be measured from the ionization produced by the particle or from its x-ray transition radiation in a homogeneous medium.

The possibilities, regions of applicability, and methods of realization of these experimental techniques have already been frequently discussed in the literature. Until recently, the ionization methods were not regarded as promising because of the weak (logarithmic) dependence of the ionizing capacity of relativistic particles on γ and its saturation for $\gamma \lesssim 10^3$, and also because of the appreciable fluctuations inherent in the ionization process. However, the rapid development of techniques for acquisition and analysis of information and progress in the methods of multiwire proportional and drift chambers, and also streamer chambers have had the consequence that these detectors now compete successfully in the region $\gamma \approx 20$–400 with other methods of particle identification (Fig. 1).[1,2]

An important advantage of such ionization–coordinate detectors is their good space resolution, which makes it possible to identify simultaneously individual secondary particles emitted in a small solid angle. It is difficult to use multisection threshold Cherenkov counters for this purpose on account of their great length (>10 m), high cost, and unsatisfactory space and angle resolution.[1] Some hope is at present placed in Cherenkov detectors in which the velocity of each secondary particle is determined from the size of the Cherenkov-radiation ring. By means of such detectors, one can identify interaction products with $p = 1$–10^2 GeV/c.[2] However, such detectors have not yet been widely used.

In recent years, we have also seen the successful development of the method of identification of relativistic particles using x-ray transition radiation in layered radiators.[1-3] Simultaneous use of the information on the energy and emission angle of the x rays, detected in

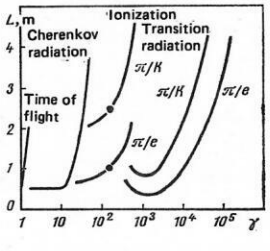

FIG. 1. Dependence of the length L of the detector needed to identify particles as a function of the Lorentz factor γ of the particles.[1] The points on the curves for the ionization identifiers correspond to a gas pressure of 1 atm.

 0090-4759/83/030270-36$04.40

drift chambers with a heavy noble gas, makes it possible to create compact identifiers of relativistic particles.[4] However, the low intensity of the x-ray transition radiation for $\gamma < 10^3$ limits the use of this method to mainly the region of large Lorentz factors.

There already exist several monographs and review papers devoted to aspects of the measurement of the ionization produced by relativistic charged particles.[1,2,5-13] However, only a few of them consider the problem of identifying high-energy particles by means of ionization detectors. The present review, which takes into account the recent achievements in this field and is based on the results of a large number of original studies, is an attempt to fill the existing gap.[1)] The data contained in it and the bibliography can also serve as reference material.

1. IONIZATION EFFECTS UNDER THE INFLUENCE OF HIGH-ENERGY PARTICLES

Primary ionization and ionization energy loss

Differential cross section of inelastic collisions. The mean number dN/dx of collisions per unit path length x (g/cm^2) of a particle in matter accompanied by the excitation and ionization of atoms of the medium is determined by the differential cross section $d\sigma_{in}/d\varepsilon$ of inelastic atomic collisions:

$$dN/dx = \frac{n_a}{\rho}\int_0^{T_{max}} (d\sigma_{in}/d\varepsilon)\, d\varepsilon = n_a\sigma_{in}/\rho, \qquad (1)$$

where n_a is the number of atoms in 1 cm^3, ρ is the density of matter (g/cm^3), ε is the energy transferred in an individual collision, T_{max} is the maximal kinematically possible value of ε, and σ_{in} is the total cross section of inelastic collisions.

To calculate $d\sigma_{in}/d\varepsilon$, it is necessary to know the wave functions of the atoms of the matter. Since correct calculations of the wave functions can be made only for atomic hydrogen and helium, more or less realistic approximate models of an atom are generally used.[12,13,15] The results of calculations of the number of inelastic collisions in gases for a model of a medium with continuous oscillator strengths calculated using data on photoabsorption cross sections are given in Table I and in Fig. 2.[13,15]

At relativistic velocities, because of the Lorentz transformation of the electromagnetic field of the particle, the radius of the region around its trajectory in which the field is sufficiently strong to excite and ionize atoms of the medium increases, and the total cross section of inelastic collisions increases as well. At the same time, an ever increasing number of atoms is subject to the influence of the particle, and their polarization leads to screening of its field and to a gradual saturation in the growth of the cross section (Fermi plateau[16]). Since the screening is stronger, the higher

TABLE I. Mean number dN/dl of inelastic collisions accompanying excitation and ionization on 1 cm of the path and the specific primary ionization dN_1/dl, their relativistic rises R_N and R_{N_1}, and the mean specific ionization energy loss $-dE/dl$ for singly charged relativistic particles in noble gases under normal conditions ($P = 1$ atm, $t = 0$°C).[13,15]

Gas	dN/dl, cm^{-1}		R_N	dN_1/dl, cm^{-1}		R_{N_1}	$(-dE/dl)$, keV/cm
	Minimum of ionization	Fermi plateau		Minimum of ionization	Fermi plateau		Minimum of ionization
He	5.28	7.97	1.51	3.50	5.17	1.48	0.365
Ne	12.73	19.31	1.52	11.75	17.77	1.51	1.653
Ar	29.28	40.68	1.39	26.65	36.80	1.38	2.879
Kr	35.41	49.97	1.41	35.41	49.97	1.41	5.417
Xe	48.13	65.32	1.36	48.13	65.32	1.36	7.871

the density of the matter, this phenomenon is frequently called the *density effect.*

Primary Ionization. The quantity

$$dN_1/dx = \frac{n_a}{\rho}\int_{I_0}^{T_{max}} (d\sigma_{in}/d\varepsilon)\, d\varepsilon \qquad (2)$$

(I_0 is the first ionization potential of the matter) corresponds to the mean number of ionizing collisions per unit path length and is called the specific primary ionization (see Table I). In accordance with the theory of atomic collisions[13,17] for high-energy single charged particles in gases, the specific primary ionization is almost independent of T_{max} and is equal to

$$dN_1/dl = \rho(dN_1/dx) = \frac{A_1}{\beta^2}\left(\frac{P}{T/273}\right)[A_2 + 2\ln\beta\gamma - \beta^2 - \delta_{N_1}]. \qquad (3)$$

Here, A_1 and A_2 are constants that depend on the properties of the matter (see the Appendix), P is the pressure (atm), T (°K) is the temperature of the gas, and δ_{N_1} is a correction for the density effect of the medium.[13,17]

At relativistic energies of the particles, the dependence of dN_1/dl on γ passes through a minimum (at $\gamma \approx 4$) and then rises logarithmically, finally reaching the Fermi plateau because of the saturation effect (Fig. 3a). The primary ionization corresponds mainly to collisions with outer atomic electrons, and its relativistic rise is

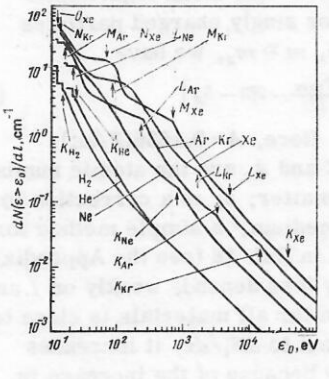

FIG. 2. Integral distribution $dN(\varepsilon > \varepsilon_0)/dl$ of energy transfers $\varepsilon > \varepsilon_0$ in inelastic collisions of a singly charged relativistic particle with atoms of the gas at the minimum of the ionization under normal conditions.[15] The arrows indicate the absorption edges of the atomic shells. When ε is higher than the K absorption edges, $dN(\varepsilon > \varepsilon_0)/dl \propto \varepsilon_0^{-1}$ (Rutherford behavior).

[1)] After the present review had been written, we became acquainted with Lyubimov's lecture published in Ref. 14, in which some of the questions touched upon here are considered briefly.

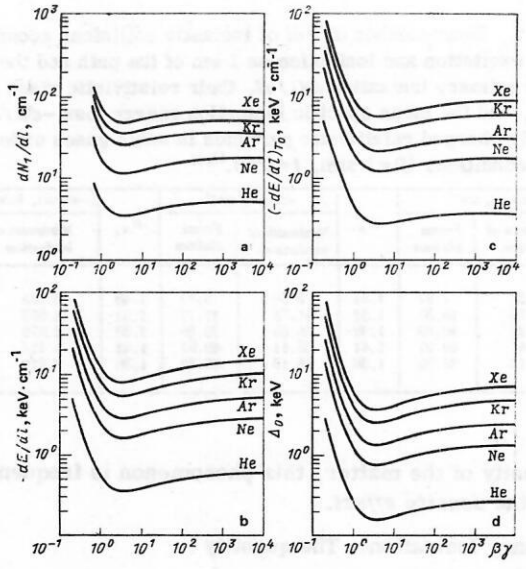

FIG. 3. Dependence of the calculated specific primary ionization dN_1/dl (Ref. 13) (a), the mean specific energy loss $-dE/dl$ of protons (b), the restricted specific energy loss $(-dE/dl)_{T_0}$ (T_0=100 keV) (c), and the probable energy loss Δ_0 (d) in a gas layer 1-cm thick[18] on $\beta\gamma$ for singly charged relativistic particles in noble gases at 1 atm and 0°C.

more pronounced, the higher the first ionization potential.[17] Therefore, in neon and helium it is greater than in argon and xenon. Calculations of dN_1/dl in accordance with (3) for noble gases agree well with the experimental data, a compilation of which can be found in Ref. 13.

Mean, restricted, and probable energy losses. The mean specific energy loss $(-dE/dx)$ on excitation and ionization of atoms of a medium (the ionization energy loss):

$$(-dE/dx) = \frac{n_a}{\rho}\int_0^{T_{max}} \varepsilon\,(d\sigma_{1n}/d\varepsilon)\,d\varepsilon \qquad (4)$$

can be calculated without any simplifying assumptions about the behavior of $d\sigma_{in}/d\varepsilon$ using just one averaged characteristic of the matter—the mean logarithmic ionization potential I. For singly charged particles heavier than the electron, $m \gg m_e$, we have

$$(-dE/dx) = \frac{A}{\beta^2}\left[\ln\frac{2m_ec^2\beta^2T_{max}}{I^2(1-\beta^2)} - 2\beta^2 - \delta_E\right] \qquad (5)$$

(Bethe–Bloch formula[5]). Here, $A = 0.1536(Z/A_0)$ MeV·g^{-1}·cm^2, in which Z and A_0 are the atomic number and mass number of the matter; δ_E is a correction for the density effect of the medium,[6] a simple method for calculating it being given in Ref. 18 (see the Appendix). The mean specific energy loss depends weakly on I and at the ionization minimum for all materials is close to 2 MeV·g^{-1}·cm^2. In contrast to dN_1/dx, it increases steadily with increasing γ because of the increase in T_{max}, and it is not subject to saturation (Fig. 3b).

The mean ionization energy loss in collisions with transfers $\varepsilon \leq T_0$ is called the *restricted energy loss.*[6] The specific restricted energy loss for singly charged relativistic particles is given by

$$\left(-\frac{dE}{dx}\right)_{T_0} = \frac{n_a}{\rho}\int_0^{T_0} \varepsilon\left(\frac{d\sigma_{1n}}{d\varepsilon}\right)d\varepsilon = \frac{A}{\beta^2}\left[\ln\frac{2m_ec^2\beta^2T_0}{I^2(1-\beta^2)} - \beta^2 - \delta_E\right], \qquad (6)$$

which is valid for $I_K \ll T_0$ (I_K is the ionization potential of shell K of the atom).[2)] This relation is confirmed, for example, in ionzation measurements in Wilson chambers,[6,13,19] in which the density of tracks (if large bunches of drops corresponding to energy transfers $\varepsilon > T_0$ are excluded) is proportional to $(-dE/dx)_{T_0}$ (see below).

The quantity T_0 is frequently determined from the range of a delta electron, which is equal to the track width or the dimension of the sensitive region of the detector, provided the contribution of the more energetic delta electrons is excluded. It should be borne in mind that some of the energy transferred to an atom can be emitted in the form of Auger electrons or fluorescence. However, the weak (logarithmic) dependence of the relation (6) on T_0 does not require accurate determination of T_0. With increasing γ, the logarithmic rise in $(-dE/dx)_{T_0}$, as in dN_1/dx, is completely compensated by the density effect, and the Fermi plateau is reached:

$$(-dE/dx)_{T_0,\,pl} = A\ln\frac{2m_ec^2T_0}{(\hbar\omega_p)^2} \qquad (7)$$

(see Fig. 3c), where ω_p is the plasma frequency of the medium:

$$\hbar\omega_p \equiv (4\pi\hbar^2 n_a Z/m_e)^{1/2} = 28.817\,(\rho Z/A_0)^{1/2}\,[\text{eV}]. \qquad (8)$$

The position at which the dependence $(-dE/dx)_{T_0}$ reaches the plateau can be nominally characterized by the Lorentz factor γ_{pl}, the meaning of which is illustrated in the Appendix. In accordance with Ref. 18, γ_{pl} is given by

$$(\beta\gamma)_{pl} = \exp\{\ln[I^2/(\hbar\omega_p)^2] - 1\} \approx 1.65\,(I/\hbar\omega_p). \qquad (9)$$

Therefore, the Fermi plateau begins later, the higher the atomic number and the lower the density of the matter. The data of Refs. 20 and 21 on the decrease in the plateau level of the restricted energy loss at very large γ due to radiation corrections were not confirmed by more careful experiments (see, for example, Refs. 8, 22, and 23) and the calculations of Ref. 24.

The escape of energetic delta electrons from the detector, and also the saturation of the detector and the electronics at very large ionization can strongly distort the measured mean energy loss. However, such effects do not influence the probable value corresponding to the maximum of the distribution of the ionization energy loss or the width of this maximum.[25,26] It is therefore necessary to measure the probable energy loss (see below) rather than the mean loss. The probable energy loss behaves with increasing γ like $(-dE/dx)_{T_0}$ (see Fig. 3d).

Mean ionization potential. The mean (logarithmic) ionization potential I of a medium can be measured by means of the decelerating capacity of the medium[6-8,11]

[2)] When $T_0 \lesssim T_k$, it must be borne in mind that collisions with electrons of deep shells do not contribute to the measured $(-dE/dx)_{T_0}$. Therefore, it is necessary to substitute the effective values of Z and I into Eq. (6).[19]

TABLE II. First, I_0, and mean, I, ionization potentials, the plasma energy $\hbar\omega_p$, and the mean energy w expended on the production of one pair of ions in the gases used in ionization detectors.

Gas	Chemical formula	Z	A_0	$\rho\cdot10^3$ (1 atm, 0°C), g/cm³	I_0, eV (Ref. 29)	I, eV (Ref. 11)	$\hbar\omega_p$, eV	w, eV (Ref. 29)**
Helium	He	2	4.0026	0.1779	24.58	42.3±0.5	0.272	42.3
Neon	Ne	10	20.183	0.897	21.56	133±3	0.608	36.4
Argon	Ar	18	39.948	1.774	15.76	188±2	0.815	26.3
Krypton	Kr	36	83.8	3.725	13.996	357±2	1.153	24.05
Xenon	Xe	54	131.3	5.837	12.127	489±9	1.412	21.9
Hydrogen	H_2	2	2.016	0.0896	15.4	18.5±0.2	0.272	36.3
Nitrogen	N_2	14	28.013	1.246	15.6	82±4	0.719	34.65
Oxygen	O_2	16	31.999	1.422	12.2	98.5±1.5	0.768	30.83
Methane	CH_4	10	16.043	0.7168	13.1	42.8	0.609	27.1
Acetylene	C_2H_2	14	26.038	1.173	11.4	59.5	0.724	25.75
Ethylene	C_2H_4	16	28.054	1.2604	10.5	50.0	0.773	25.8
Ethane	C_2H_6	18	30.070	1.3566	11.6	47.2	0.813	24.4
Carbon dioxide	CO_2	22	44.011	1.9769	13,8	85.6	0.906	32.8
Propane	C_3H_8	26	44.097	2.0096	11.2	49.0	0.992	23.45
Isobutane	$i-C_4H_{10}$	34	58.125	2.673	10.6	50.0	1.139	23.2
Freon-12	CCl_2F_2	58	120.91	5.398	11.7	139.0	1.467	29.55
Freon-13	$CClF_3$	50	104.46	4.663	13.1	126.0	1.361	—
Freon-13B1	$CBrF_3$	68	148.91	6.648	—	196.9	1.588	—
Sulfer hexafluoride	SF_6	70	146.05	6.520	15.7	131.7	1.611	—
Water	H_2O	10	18.015	0.017*	12.6	69.8	0.089*	29.9
Ethyl alcohol	C_2H_5OH	26	46.070	0.108*	10.5	59.2	0.225*	—
Methylal	$(CH_3O)_2CH_2$	42	76.096	—	—	64.0	—	—

*For saturated vapor at 20°C.
**For β electrons in pure gas.

and calculated from the energy dependence of the photoabsorption cross section.[11,13] The recommended values of I for some elements[11] and chemical compounds used in gas ionization detectors are given in Table II. At $\beta \approx 1$, an error of 15% in the value of the mean ionization potential changes $-dE/dx$ by only 1–2%. Therefore, to estimate the I of elements one can use the approximate empirical expressions of Ref. 27:

$$I/Z[\text{eV}]=\begin{cases}12+7/Z, & Z\leqslant 13;\\ 9.76+58.8Z^{-1,19} & Z>13,\end{cases} \tag{10a}$$

or[28]

$$I[\text{eV}]=\begin{cases}11.2+11.7Z, & Z\leqslant 13\\ 52.8+8.71Z, & Z>13.\end{cases} \tag{10b}$$

The additivity within about 2% of the decelerating capacities of elements (or materials) occurring in chemical compounds (or mixtures)—the Bragg rule—makes it possible to calculate the values of I for gaseous compounds (or mixtures):

$$\ln I=\sum_i a_iZ_i\ln I_i/\sum_i a_iZ_i. \tag{11}$$

Here, a_i, Z_i, and I_i are the number of atoms in a molecule of the compound (or the relative partial pressure) and the atomic number and mean ionization potential of element i (or the i-th component of the mixture). To calculate the ionization energy loss in a gaseous chemical compound (or mixture) in accordance with (5)–(8), it is necessary to substitute in them the values

$$\left.\begin{aligned}&Z=\sum_i a_iZ_i,\ A_0=\sum_i a_iA_{0i};\\ &\rho=1.219\cdot10^{-2}A_0P/(T/273).\end{aligned}\right\} \tag{12}$$

Energy loss and measured ionization. The ionization energy loss of charged particles is usually measured by the ionization effect dJ/dx produced by them, i.e., from the density of the structural elements of the track—grains, drops, bubbles, bunches, streamers, etc. (in track detectors) or from the collected electric charge (in electronic detectors). The observed ionization effect depends not only on the properties of the particle itself (m, z, v) or the material of the detector (Z, A_0, ρ), but also on the mechanism of operation of the detector, which determines the weight $\mathscr{P}(\varepsilon)$ with which each collision contributes to the total ionization effect.[13] The weight function $\mathscr{P}(\varepsilon)$ depends on the energy ε transferred in the collision. Thus,

$$dJ/dx=\frac{n_a}{\rho}\int_0^{T_0}\mathscr{P}(\varepsilon)\,(d\sigma_{1n}/d\varepsilon)\,d\varepsilon. \tag{13}$$

In detectors in which $\mathscr{P}(\varepsilon)$ is proportional to ε (Wilson chambers, ionization chambers, scintillation, semiconductor, and proportional detectors), the ionization effect is also proportional to the specific energy loss. Indeed, if $\mathscr{P}(\varepsilon)=\varepsilon/w$, where w is the mean energy expended on the formation of one pair of ions[3)] (see Table II), which is effectively independent of the mass, charge, and velocity of the particle,[29] then

$$dJ/dx=\frac{n_a}{\rho}\int_0^{T_0}\frac{\varepsilon}{w}\,(d\sigma_{1n}/d\varepsilon)\,d\varepsilon=\frac{(-dE/dx)_{T_0}}{w}. \tag{14}$$

But if $\mathscr{P}(\varepsilon)$ is a step function of ε, then the observed ionization effect is proportional to the number of collisions with energy transfers above the threshold (detectors of primary ionization, bubble chambers[13]). The intermediate case when $\mathscr{P}(\varepsilon)$ is a nonlinear function of ε corresponds to nuclear photoemulsions.[13]

Identification of high-energy particles using the relativistic rise of the ionization. The ionization methods

[3)] In mixtures containing additives with ionization potentials below the excitation potentials of the main gas, w is smaller than for each of the components (Jesse effect). This effect depends on the concentration of the additive. For example, in mixtures of argon with C_2H_6 or C_3H_8 the minimal values $w=24.4$ eV and $w=23.6$ eV correspond to molar concentrations 4% and approximately 1% of C_2H_6 and C_3H_8, respectively.[30]

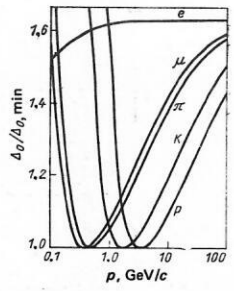

FIG. 4. Dependence of the relative probable energy loss $\Delta_0/\Delta_{0,\min}$ in 1 cm of the mixture 80% Ar + 20% CH_4 under normal conditions on the momentum p of singly charged relativistic particles. The ionization minimum corresponds to $\Delta_0 \approx 1.3$ keV.[31]

of identifying high-energy particles ($\gamma \gtrsim 10$) are based on the logarithmic rise of the measured ionization (the ionization effect) with increasing γ. The possibilities of identifying individual relativistic particles, whose momentum or energy are measured independently, are determined by the following factors:

1) the scale of the relativistic rise R of the ionization (the ratio of dJ/dx on the plateau and at the minimum) and the Lorentz factor γ_{pl} corresponding to the beginning of the plateau;

2) the fluctuations of the ionization and the relative rms error of measurement of the ionization of an individual relativistic particle (see Secs. 2 and 3);

3) the mass m of the particle. The greater the difference between the masses of particles, the easier is their identification (Fig. 4).

The values of R and γ_{pl} in various materials used in ionization detectors are given in Table III, from which it can be seen that from the point of view of the identification of high-energy particles gas detectors are the most promising and, to a lesser degree, heavy-liquid bubble chambers, nuclear photoemulsions, and solid-state detectors with large Z.

TABLE III. Relativistic rise of the ionization R and the position γ_{pl} of the transition to the plateau in different materials used in ionization detectors.

State of the matter	Detector	Substance	R	γ_{pl}
Gaseous ($P = 1$ atm, $t = 0°C$)	Gas ionization detectors using noble gases, multiatomic gases, and mixtures of them (Wilson, ionization, proportional, and drift chambers*)[6,13,15]	He	1.55	260
		Ne	1.59	360
		Ar	1.59±0.05	380
		Kr	1.71±0.09	510
		Xe	1.75±0.05	570
		C_3H_8	1.3±0.3	80
Condensed	Bubble chambers** (Ref. 13)	H_2	1.01	10
		C_3H_8	1.13±0.03	100
		$CBrF_3$	1.32±0.05	50
	Nuclear photoemulsions** (Refs. 8, 13, and 22)	AgBr	1.06—1.15	70
	Scintillation detectors (Refs. 8 and 13)	$(CH)_n$	1.01—1.02	5
		NaI (Tl)	1.11—1.14	20
	Semiconductor detectors[8]	Si	1.1	10

*Probable ionization in a layer of gas 2-cm thick. The results for helium and neon were obtained by the Monte Carlo method.[15]
**Because of the nonlinear behavior of the function $\mathscr{P}(\varepsilon)$, the ionization effect is not proportional to $-dE/dx$.[13]

Fluctuations of the ionization; the probable ionization

The nature of the fluctuations of the ionization. The ionization measured in gas ionization detectors arises as a result of random inelastic collisions of the charged particle with atoms of the medium and is subject to appreciable fluctuations, which are made up of: a) Poisson fluctuations in the number of inelastic collisions, with mean value $N = x(dN/dx)$ (see Table I); b) the spread in each primary collision of the energy transfers ε (see Fig. 2), the sum of these giving the energy loss Δ in a layer of thickness x; c) the fluctuations in the number of secondary pairs of ions for fixed energy release ε. These fluctuations have dispersion $F(\varepsilon/w)$ (where ε/w is the mean number of secondary pairs of ions; $F < 1$ is the Fano factor[32]) and are somewhat smaller than the purely random (Poisson) fluctuations; d) fluctuations which arise during the collection and amplification of the charge released in the volume of the detector and determine the instrumental resolution.

The total relative rms spread of the pulse height in gas proportional detectors associated solely with fluctuations of type c) and d) for $\Delta = \text{const}$ is[33]

$$\sigma_a = (\Delta/w)^{-1/2} \qquad (15)$$

and for $w = 30$ eV is about 7% for the 5.9-keV line of ^{55}Fe (the relative instrumental half-width is $W_a = 2.355\sigma_a \approx 17\%$). The instrumental errors only slightly broaden the curve of the ionization fluctuations, and its form is in fact determined by the distribution of the energy loss, i.e., by processes a) and b).

The fluctuations of the primary ionization correspond to a Poisson distribution with mean value $N_1 = x(dN_1/dx)$ (see Table I).

Fluctuations of the energy loss. The distributions of the ionization energy loss have the form of asymmetric bell-shaped curves. Their shape and probable value depend on the velocity and charge of the particle, and also on the atomic number, density, and thickness of the matter. Transformation of the Poisson distribution of the primary ionization into the asymmetric distribution of the total ionization can be observed during change in the regime of operation of a streamer chamber[34] (Fig. 5).

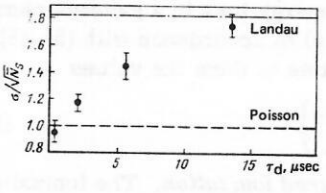

FIG. 5. Dependence of the rms deviation σ of the number $\bar{N}_s$ of streamers over 5-cm track length (in units of the standard Poisson deviation) on the delay time τ_d. The streamer chamber is filled with helium to pressure 0.4 atm and irradiated with relativistic electrons of energy $1.3\ \text{MeV} \leq E \leq 2.26\ \text{MeV}$.[34]

The nature of the distribution $f(x, \Delta)$ of the ionization energy loss of fast charged particles ($\Delta \ll E$) depends on the ratio

$$\varkappa = \xi/T_{\max}. \tag{16}$$

The physical meaning of the quantity

$$\xi = Ax/\beta^2 \tag{17}$$

can be explained as follows. At large (compared with the characteristic binding energy I of the atomic electrons) energy transfers, when the collisions are of Rutherford type, i.e., when

$$d\sigma_{in}/d\varepsilon = A\rho/n_a\beta^2\varepsilon^2, \tag{18}$$

there is on the average one collision in which $\varepsilon > \xi$ in the layer of thickness x. Thus, $\varkappa$ is a measure of the contribution of collisions with $\varepsilon \sim T_{max}$ and, simultaneously, a measure of the thickness of matter.

The solution to the problem of the fluctuations of the ionization energy loss in general form was first formulated by Landau.[35] Vavilov[36] calculated the corresponding distribution for the case $0.01 < \varkappa \lesssim 1$.[4)] For $\varkappa \gg 1$, the Vavilov distribution goes over into a symmetric Gaussian distribution,[38] and for $\varkappa < 0.01$ into the Landau distribution, which corresponds to a thin layer of matter.

Energy loss in thin layers. The Landau distribution. The Landau distribution is calculated under the assumption that the ionization energy losses in collisions in which $\varepsilon \lesssim I$ are fixed and equal to the mean losses, the fluctuations being entirely determined by the collisions with $\varepsilon \gg I$, whose cross section corresponds to the Rutherford formula (18). This means that the number of collisions with energy transfers $\varepsilon \lesssim I$, whose contribution is measured by the ratio ξ/I, is very large:

$$\xi/I \gg 1. \tag{19}$$

The distribution of the ionization energy loss calculated by Landau is an asymmetric function $\varphi(\lambda)$, where

$$\lambda = (\Delta - \Delta_0)/\xi - 0.225 \tag{20}$$

with a slowly ($\propto \lambda^{-2}$) decreasing "tail" in the region of large λ (Fig. 6). Its probable value $\lambda_0 = -0.225$ and full width at half maximum (half-width) $\delta = 3.98$ correspond, respectively, to the probable value Δ_0 and half-width $\delta = 3.98\xi$ of the distribution $f(x, \Delta)$. The Landau distribution is tabulated in Ref. 39 and can be approximated[15] by the complicated function of Moyal.[40] The probable ionization energy loss Δ_0 is given by[5)]

$$\Delta_0 = \xi\left[\ln\frac{2m_ec^2\beta^2\xi}{I^2(1-\beta^2)} - \beta^2 + 0.198 - \delta_E\right]. \tag{21}$$

At very large γ, it reaches saturation:

$$\Delta_{0,pl} = \xi \ln [2m_ec^2 \cdot 1{,}22\xi/(\hbar\omega_p)^2]. \tag{22}$$

These last expressions agree with (6) and (7) for the restricted energy loss in a layer of thickness x and $T_0 = 1.22\xi$. In gases, the minimum of Δ_0 is at $\gamma \approx 4$ and is

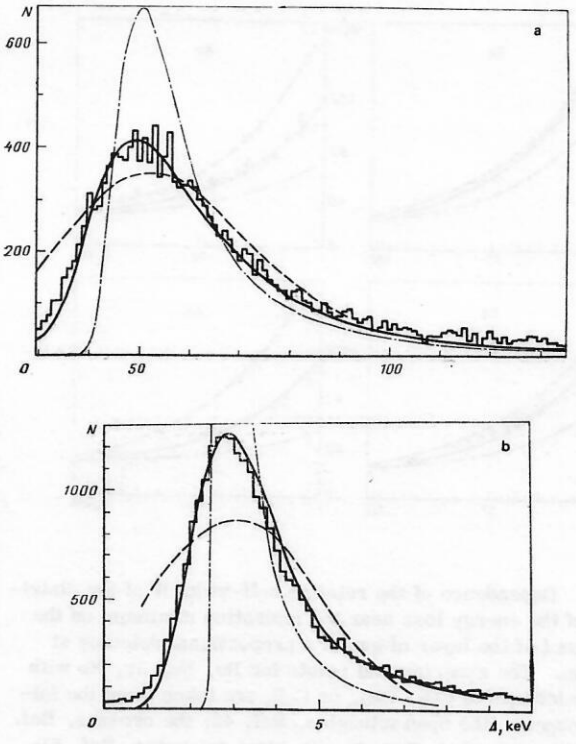

FIG. 6. Distributions of the energy loss at the ionization minimum at $P = 1$ atm (a) for protons, $p = 2.1$ GeV/c, $l = 5$ cm, mixture 95% Ar + 5% CH_4 (the channel number is plotted along the abscissa),[58] and on the Fermi plateau (b) for electrons, $p = 3$ GeV/c, $l = 5$ cm, mixture 93% Ar + 7% CH_4.[51] The continuous, chain, and broken curves represent simulation by the Monte Carlo method,[15] Landau's theory,[35] and the Blunck–Leisegang theory,[67] respectively.

almost independent of I (eV), the pressure P (atm), and length l (cm) of the detector. The expected relativistic rise R of the probable energy loss in a gas is in accordance with (22) and (21)

$$R = \frac{\Delta_{0,\,pl}}{\Delta_{0,\,min}} \approx \frac{0.9375\,(\ln l + 19.2575)}{[\ln Pl - \ln (I^2/Z) + 17.7965]}, \tag{23}$$

and is larger, the heavier the gas and the lower its pressure.

The relation (19) indicates that one cannot apply Landau's theory for very thin absorbers, when $\xi/I \approx 1$. Thus, substituting $I \approx 13.5Z$ and $x = \rho l$ in (19) for an estimate, we find that in gases this theory is valid only when

$$Pl\ (\text{atm. cm}) \gg 2\beta^2. \tag{24}$$

Therefore, it is not in a position to describe the distribution of the energy loss of relativistic particles in the thin layers ($Pl \lesssim 10$) of gas characteristic of proportional detectors.

Numerous measurements made since the fifties by means of proportional counters and chambers in the investigation of not only cosmic rays[42-46] but also high-energy particles from accelerators[47-64] clearly demonstrated that the fluctuations of the energy loss in thin layers of gas are appreciably greater than the fluctuations predicted by Landau's theory (Figs. 6 and 7). In addition, in heavy gases when $Pl \lesssim 10$ collisions with

[4)] A similar distribution, obtained earlier by Symon,[37] is given in Ref. 5.

[5)] The constant $0.198 = \ln(1.22)$ is determined more accurately in Ref. 41. In Landau's original paper it is equal to 0.373.

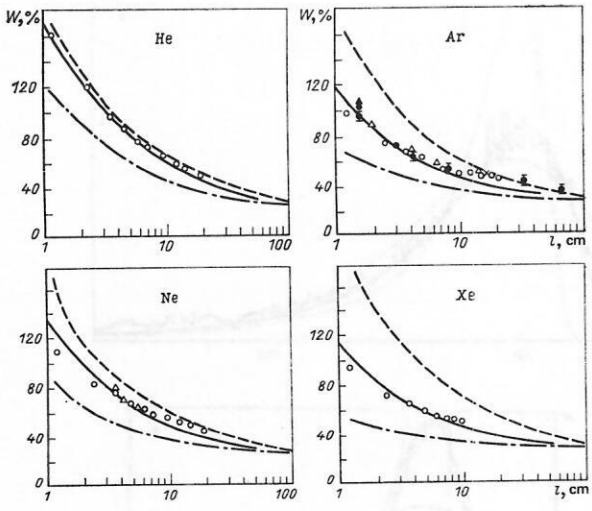

FIG. 7. Dependence of the relative half-width W of the distribution of the energy loss near the ionization minimum on the thickness l of the layer of gas of a proportional detector at $P=1$ atm. The experimental points for He, Ne, Ar, Xe with 5–10% additions of CO_2, CH_4, or C_3H_8 are taken from the following papers: the open triangles, Ref. 42; the crosses, Ref. 47; the black circles, Ref. 50; the black triangles, Ref. 51; the black circles with bar, Ref. 52; and the open circles, Ref. 55. The chain, broken, and continuous curves are the Landau distribution,[35] the Blunck–Leisegang distribution,[67] and the prediction of the harmonic-oscillator mode,[69] respectively. The calculated curves are corrected for the instrumental resolution of the detector.

electrons of deep atomic shells do not contribute to the energy loss near the probable value, since the binding energy[6)] of these electrons is $\varepsilon_{K,L} \gtrsim \Delta_0$.[15,65] Therefore, the measured values of Δ_0 and R are somewhat lower than the expected values (Figs. 8 and 9). As follows from (24), the agreement with Landau's theory improves with increasing thickness of the gas layer (Figs. 7 and 8).

The results of the experiments[42,44,63] and simulation[15] indicate a universal dependence of the width of the energy-loss distribution on the parameter ξ/I for all

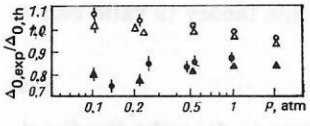

FIG. 8. Dependence of the ratio of the measured $\Delta_{0,\exp}$ (Ref. 62) and calculated $\Delta_{0,\text{th}}$ (Ref. 35) probable energy loss of electrons ($p=0.3$ GeV/c) on the gas pressure P in proportional detectors filled with the mixture 90% Ar + 10% CH_4. The experimental points represented by the black circles correspond to $l=9$ cm; the black triangles, to $l=10$ cm; the open circles, to $l=90$ cm; and the open triangles, to $l=100$ cm.

6)Thus, in 1 cm of argon or xenon at $P=1$ atm and $t=20$ °C the values are $\Delta_{0,\min}=1.22$ keV and 3.61 keV, respectively. At the same time, the energies of the L and K absorption edges in argon are $\varepsilon_L=0.86$ keV and $\varepsilon_K=4.8$ keV, and in xenon they are $\varepsilon_L=4.8$ keV and $\varepsilon_K=34.6$ keV.

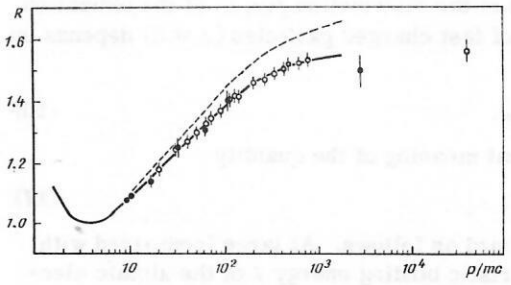

FIG. 9. Dependence of the relativistic rise R of the probable ionization measured in the 128-layer EPI detector ($l=6$ cm, 95% Ar + 5% CH_4, $P=1$ atm, $T=0$ °C) on p/mc.[61] The broken curve corresponds to Landau's theory[35] with correction for the density effect of the medium.[18]

gases (Fig. 10). In the interval $0.3 \lesssim \xi/I \lesssim 30$, the relative half-width $W=\delta/\Delta_0$ for relativistic particles is[12]

$$W = 0.81\,(\xi/I)^{-0.32} \approx 0.44\,[(I/Z)/Pl]^{0.32}. \qquad (25)$$

Therefore, for $Pl=$ const the fluctuation curve will be narrower, the smaller is I/Z. Small values of I/Z are characteristic of multiatomic gases (propane, isobutane, etc.) consisting of light elements (see Table II). Thus, one can expect[66] an energy-loss distribution in these gases narrower than in argon or xenon, and this is confirmed experimentally.[63] This fact can be explained by the influence of the deep electron shells, which cause an increase in the spread of the energy transfers in individual collisions and, accordingly, of the fluctuation of the ionization energy loss in heavy gases (see Fig. 2).[12,15,63]

The narrowing of the fluctuation curves in multiatomic gases must be taken into account in the design of ionization identifiers of relativistic particles. The optimal choice of Z and Pl of the gas corresponds to not only the maximal relativistic rise but also a small half-width W. These conditions are mutually contradictory, since the first means that I^2/Z is large and Pl (23) is small, while the second requires large Pl and small I/Z (25). Therefore, the decisive criterion in the choice of the gas is the best separation of the particles with respect to their mass.

Modifications of Landau's theory. Blunck and Leisegang[67,68] extended Landau's theory. They introduced corrections to take into account the binding of electrons in atoms and showed that when

$$b^2 = 20\,(\text{eV})\,Z^{1/3}\overline{\Delta}/\xi^2 \gg 3, \qquad (26)$$

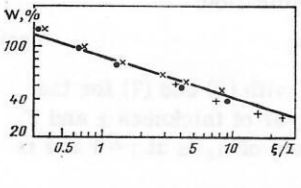

FIG. 10. Dependence of the relative half-width W of the energy-loss distribution in gases on ξ/I for $p=3.5$ GeV/c. The crosses are the experimental data for Xe, the black circles for Ar, and the plus signs for C_3H_8.[63] The continuous line is the dependence (25).

where $\bar{\Delta} = x(-dE/dx)$, the fluctuations of the energy loss are appreciably greater than the width of the Landau distribution and can be approximated by the sum of four Gaussian distributions:

$$f(x, \Delta)\, d\Delta = \xi \sum_{i=1}^{4} \frac{c_i \gamma_i}{(\gamma_i^2 + b^2)^{1/2}} \exp\left[-\frac{(\lambda - \lambda_i)^2}{\gamma_i^2 + b^2} \right] d\lambda. \qquad (27)$$

(The values of c_i, γ_i, and λ_i are calculated in Ref. 67.) For $b^2 \ll 3$, this distribution goes over into Landau's distribution. The Blunck–Leisegang theory gives a reasonable description of the experimental data for $\xi/I > 10$. However, for $\xi/I \approx 1$ it appreciably overestimates the width of the fluctuation curve (see Figs. 6 and 7).

A simple model for calculating the energy-loss distributions in very thin layers of matter, when $N \gtrsim 10$, was proposed by Ermilova and Chechin.[69] In their model, the atomic electrons are treated as independent isotropic harmonic oscillators with eigenfrequency $\omega = I/\hbar$. This makes it possible to calculate the differential cross section $d\sigma_{in}/d\varepsilon$ corresponding to all excitation multiplicities and, by substituting it in Landau's general solution, to find the energy-loss distribution function. The results of the calculations based on the harmonic-oscillator model when the correction for the polarization of the medium is small agree well with the experimental data down to $Pl \approx 1$, which corresponds to $\xi/I = 0.5$–1 (see Fig. 7). The energy loss in the region of the Fermi plateau is described somewhat less well by this model, since it underestimates the polarization capacity of the atoms, which depends primarily on the outer electron shells with low ionization potentials of order 10–50 eV.

Other attempts have been made to develop Landau's theory with the aim of obtaining an analytic solution for $f(x, \Delta)$ in thin layers of gas.[70,71] These have also substituted into Landau's general solution the differential cross section of inelastic collisions corresponding to the model of a polarizable medium with discrete oscillator strengths. The results of these calculations agree with the experimental data but entail lengthy computer calculations, these being just as complicated as simulation by the Monte Carlo method.

The limits of applicability of the various theories that describe the distributions of the ionization energy loss are illustrated in Table IV.

Simulation of the energy loss by the Monte Carlo method. Simulation of the ionization energy loss is a "computer experiment" in which one follows in detail the passage of ionizing particles through a medium. For this, proceeding from the known cross section $d\sigma_{in}/d\varepsilon$ of inelastic collisions, one finds both the number of collisions per path length x [corresponding to a Poisson distribution with mean value $N = x(dN/dx)$] and the energy transfer ε in each individual collision with allowance for excitation and ionization of the atoms (see Fig. 2). The sum of all the energy transfers in the layer x gives the required energy loss. Repeating the described procedure many times by means of a fast computer, one can readily accumulate the "statistics" needed to construct the fluctuation curve.

TABLE IV. Region of applicability of theories that describe the distributions of the ionization energy loss.[13]

$\varkappa = \xi/T_{max}$	ξ/I	References (in square brackets)
$\gg 1$	$\gg 10^2$	[38]
$\gtrsim 1$	$> 10^2$	[36,37,72]
$10^{-2} \leqslant \varkappa \leqslant 1$	> 10	[73]
$\leqslant 10^{-2}$	$> 10^2$	[35]
$< 10^{-2}$	> 10	[67,68]
	~ 1	[69—71]
$\ll 1$	$\ll 1$	The energy-loss distribution function $f(x, \Delta = \epsilon)$ is proportional to the differential cross section $d\sigma_{in}/d\epsilon$ of inelastic collisions

Simulation of the energy loss was begun comparatively recently[15,65,74-76] after the appearance of data on the dependence $d\sigma_{in}/d\varepsilon$. This method makes it possible to take into account purely experimental effects such as the influence of diffusion of electrons on the collection of charge in neighboring channels,[65] the amplitude and time resolution of the instrument, and so forth. Because of this, close agreement between the results of the calculations and experiments is achieved (see Fig. 6).

2. IDENTIFICATION OF PARTICLES BY REPEATED MEASUREMENT OF THE IONIZATION

Improvement in the accuracy of measurements in multilayer ionization detectors

Why multilayer detectors? As the length of the detector and the gas pressure are increased, the distribution of the energy loss becomes narrower very slowly, so that even when $Pl \gtrsim 10^2$ ($\xi/I \gtrsim 50$) its half-width W is 20–30% (see Fig. 7). Therefore, separate identification of relativistic hadrons in a single-layer detector is impossible at reasonable values of P and l. The way out of the dilemma is to use repeated measurement of the ionization produced by the same particle by means of several detectors or, more conveniently, a single multilayer detector. If the number n of its layers is sufficiently large, then the obtained probable value of the energy-loss distribution will be a much more accurate measure of the ionizing capacity of the particle than what is provided by measurement in a single layer of the total thickness. Since the cost of an ionization detector is approximately proportional to n, it is important to optimize the number and thickness of the layers which ensure the amplitude resolution 2–3% needed to discriminate relativistic particles at the smallest length $L = nl$ of the detector. The solution of this problem depends on the efficiency of the method used for the statistical analysis of the results of the measurements.

Multiple ($n = 2$) ionization measurements with a corresponding procedure of statistical analysis were first

used by Alikhanian, Alikhanov, and Nikitin[77] in an investigation of the composition of cosmic rays at mountain altitudes. In the following years, multilayer detectors consisting of two[78-80] and four or five[81] layers were used, and effective methods were proposed for the statistical analysis of multiple ionization measurements.[78-83] In 1956, a group at the Institute of Theoretical and Experimental Physics tested a 50-layer proportional detector designed for the identification of relativistic hadrons.[81] But it was only with the appearance of cheap semiconductor electronics at the beginning of the seventies that multilayer ionization detectors began to be used to identify high-energy particles in accelerator and cosmic-ray experiments.

Statistical analysis of measurements in a multilayer detector. Several methods of statistical analysis yielding the value of the probable ionization on the basis of measurements in a multilayer detector consisting of independent identical layers are known.

Arithmetic-mean method (Refs. 26, 47, 49, 78, 80, 81 and 84). Suppose for a distribution $\varphi(\lambda)$ of arbitrary form the integral

$$\int_{-\infty}^{+\infty} \lambda^2 \varphi(\lambda)\, d\lambda \qquad (25')$$

converges; then in accordance with the central limit theorem of probability theory (see, for example, Ref. 85) the mean values of n random samples of $\varphi(\lambda)$ satisfy a normal distribution with half-width $n^{1/2}$ times less than the original distribution. This proposition does not apply to Landau's distribution, for which the "tail" decreases in proportion to λ^{-2} and the integral (25′) diverges. Therefore, the arithmetic mean of the results of measurements of the energy loss in n layers each of thickness l is effectively equivalent to one measurement in a layer of thickness nl. The error of measurement decreases with increasing n by only $(1-\ln n/10)^{-1}$ times.[81]

To raise the efficiency of the arithmetic-mean method, it is necessary to "symmetrize" the fluctuation curve by eliminating its high-energy part, which yields little information about the probable energy loss. For the remaining $n_\alpha = \alpha n$ ($\alpha \leq 1$) measurements, the central limit theorem will be valid, and the distribution of their arithmetic-mean values will be Gaussian.[81,86] Then the accuracy in the measurement of Δ_0 is improved by $n_\alpha^{1/2}$ times, since the half-width of the Gaussian distribution is $\delta_n = \delta/n_\alpha^{1/2}$, the relative half-width is $W_n = \delta_n/\Delta_0 = W/n_\alpha^{1/2}$, and the standard deviation is $\sigma_n = W_n/2.355$. The above idea is realized by the *distribution-cutoff method* in one of the following ways.

1. Pulses with height below a given discrimination level are averaged.[47,84] This simple method is not suitable for the identification of particles, since the area of the truncated part of the fluctuation curve will depend on γ and the results of the averaging of the remaining pulses give a distorted Δ_0 value.

2. The fluctuation curve is truncated at a level at which a previously specified ratio of the cutoff boundary to the mean value of the remaining part of the distribution is constant and lies between 1.5 and 2. The arithmetic mean of the remaining measurements is proportional to the probable value of the original distribution. Such a procedure requires altogether two or three successive approximations.[82]

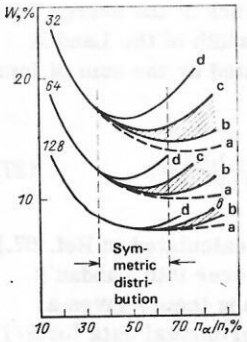

FIG. 11. Calculated relative half-width W of the energy-loss distribution in the case of analysis by the truncation method (choice of the n_α smallest pulses from n). Curves a, b, c, and d correspond to different relative excursions of the pulse heights beyond the range of the measurements: a) 0%; b) 6.2%; c) 12.5%; d) 25%. The hatched region corresponds to the real conditions of the experiment, and the numbers next to the curves give the number n of layers ofthe detector.[52]

3. The n_α smallest values are averages (Refs. 47, 49, 52–54, 59, 61, 65, 74, 76, 81, 84, and 86). In the interval $0.3 \leq \alpha \leq 0.7$, the accuracy of this method depends weakly on α (Fig. 11). Depending on the shape of the real fluctuation curve, the best accuracy corresponds to $\alpha = 0.4-0.5$ (Ref. 86) and $\alpha = 0.35-0.65$ (Ref. 52). The arithmetic-mean (truncated mean) Δ_α for the n_α minimal values is proportional to Δ_0.[63] (For $n = 200$, $\Delta_{\alpha=0.4} = \Delta_0$.[50]) This method is distinguished by simplicity and high efficiency. Its limiting case $n_\alpha = 1$, corresponding to the choice of the minimal value, is effective only for $n < 15$ (Ref. 52) and was used only in the early studies.[78,80,87]

Geometric-mean method.[49,81,84] The method is based on symmetrization of the Landau distribution in the scale of $\log\Delta$.[81] The mean value of $\log\Delta_i$ ($i = 1, 2, \ldots, n$) is proportional to $\log\Delta_0$, i.e.,

$$\left(\prod_{i=1}^{n} \Delta_i\right)^{1/n} \propto \Delta_0.$$

In this method, information from all layers is used. Unfortunately, its efficiency is not very high.

The method of rank statistics.[83,84,88] If the results of n measurements of the energy losses Δ_{ij} in a multilayer detector are arranged for each particle j in rank, i.e., in ascending order, $\Delta_{1j} < \Delta_{2j} < \ldots < \Delta_{nj}$, then for a certain fixed i the width of the distribution of the Δ_{ij} values is minimal.[84] The narrowest distribution corresponds to Δ_{ij} values near Δ_0. Thus, for $n = 10$ ($l = 1.5$ cm) the optimal value i corresponds to $i = n/3 \approx 3$. At the same time, the relative width of the fluctuation curve decreases from 100 to 46% (Table V). The width of the distribution of rank i in the interval $i = n/4-n/2$ varies weakly, which indicates its insensitivity to the shape of the original distribution. For $n > 20$, it is ex-

TABLE V. Efficiency of the methods of statistical analysis of the results of measurements in multilayer ionization detectors.

Method of statistical analysis	Ratio of errors of the measurements in an n-layer detector and a single-layer detector		
Arithmetic mean of n	0.74	0.53	—
Geometric mean of n	0.55	—	—
Minimal of n	0.55	—	—
Arithmetic mean of the n_α smallest	0.46 ($n_\alpha=7$)	—	0.168 ($n_\alpha=25$)
Method of rank statistics (rank i)	0.46 ($i=4$)	0.26 ($i=8$)	0.179 ($i=20$)
Method of maximal likelihood	0.40	0.24	0.162
Limiting value, $n^{-1/2}$ (for normal distribution)	0.333	0.204	0.131
Thickness of layer l, cm	1.5 10	1.5 24	4 62
Reference	[84]	[84]	[53]

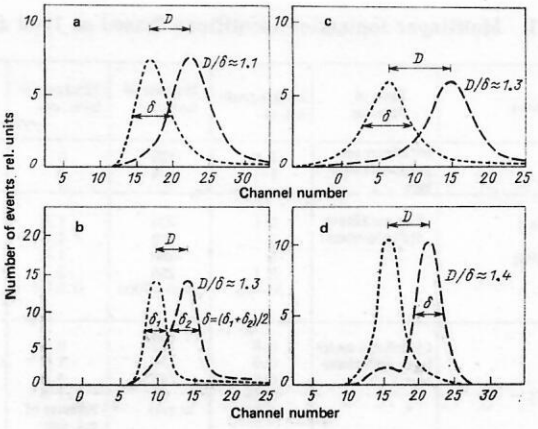

FIG. 12. Identification of electrons and pions with momentum 374 MeV/c in a 30-layer proportional detector, analyzed by different methods.[49] a) Arithmetic-mean method; b) geometric-mean method; c) truncation method ($n_\alpha/n=1/3$); d) method of maximal likelihood.

pedient to combine layers in several identical groups, apply the method of rank statistics within each group, and average the obtained results.[84]

Method of maximal likelihood[7] *(Refs. 13, 26, 52–54, 61, 79–81, and 84.* This method is the most general and most effective (i.e., has the smallest dispersion of the estimate) method of estimating the parameters of the distribution of a random variable,[85] in the considered case the probable energy loss Δ_0, corresponding to a previously known normalized distribution $f(x, \Delta, \Delta_0)$. As "effective" estimate of Δ_0 one chooses the value corresponding to the maximum of the likelihood function[79–81]

$$\mathcal{L}=\prod_{i=1}^{n} f(x, \Delta_i, \Delta_0).$$

This function is obtained by multiplying the transformed distributions $f(x, \Delta, \Delta_0)$ with maxima at the points Δ_i.[80]

A simpler application of the method consists of calculating the likelihood ratio

$$\mathcal{L}_{12}=\prod_{i=1}^{n} \frac{f_{m1}(x, \Delta_i, \Delta_0)}{f_{m2}(x, \Delta_i, \Delta_0)}, \qquad (28)$$

where f_{m1} and f_{m2} correspond to particles with masses m_1 and m_2. The case when $\mathcal{L}_{12}\gg 1$ corresponds to particles with mass m_1, and $\mathcal{L}_{12}\ll 1$ to particles with mass m_2. For $\mathcal{L}_{12}\approx 1$ there is an indeterminacy whose extent depends on how well it is possible to distinguish the distributions $\mathcal{L}_{12}$ for pure beams of particles of the same momentum with masses m_1 and m_2.

An advantage of the method of maximal likelihood is that, using all the available information, it gives the minimal width of the distribution of the estimates; its shortcoming is its sensitivity to the shape of the original distribution.

The effectiveness of the various methods of statistical analysis of the results of measurement of ionization in multilayer detectors is illustrated in Table V and in Fig. 12. The method of maximal likelihood is the most efficient. Close to it are the methods of rank statistics and distribution truncation (the n_α smallest of the n measurements). The geometric- and arithmetic-mean methods have the least efficiency. An important condition of applicability of the methods described above is the absence of correlations between neighboring layers of the ionization detector, which has been verified experimentally.[49,52,59,65]

Multilayer ionization–coordinate detectors

Types of multilayer detectors. Multilayer ionization–coordinate detectors ensure a three-dimensional reconstruction of events with high multiplicity and make it possible to identify secondary charged particles. This new class of instruments, which are called *pictorial chambers* or *image chambers*, represents the peak of modern experimental technique for detection of relativistic charged particles. The multilayer ionization–coordinate detectors can be divided into three types: proportional chambers, flat drift chambers, and cylindrical drift chambers.

Instruments of the first and second type are generally used as external identifiers of charged relativistic particles in magnetic spectrometers in conjunction with some external detector, which is most frequently a bubble chamber. Cylindrical drift chambers are used in colliding beams as vertex detectors of charged particles.

The basic parameters of operating and planned ionization–coordinate detectors are given in Table VI. In order to recognize hadrons (π, K, p) by means of such detectors, pulse-height resolution better than 3–3.5% (see above) is needed. Therefore, chambers such as, for example, PION, JADE, AFS, and ARGUS make it possible to separate only electrons from hadrons, or, in the best case, pions from protons. In the lower part of Table VI we give the parameters of the multilayer cylindrical chambers in which pulse-height analysis is not made.

[7] In Ref. 79, Behrens method; in Refs. 80 and 81, the "universal" method.

TABLE VI. Multilayer ionization identifiers (based on 1980 data).

Detector	Type of detector	Length (radius), m	Number of layers n	Thickness of layer, cm	Pressure of gas, atm	Number of channels of electronics	Calculated pulse-height resolution σ_n, %
EPI [52]	Multilayer proportional chambers	7.6	128	6	1	4096	2.6
Pion H [89]		1	24	3	0.7	792	7.0
ISIS-2 * [54,90]	Flat multilayer drift chambers	5.1	320	1.6	1	320	2.8
CRISIS [91]		3	192	1.6	1	384	3.4
Astron* [92]		5	250	1.6	1	330	2.8
IKS** [93]		5.1	256	2	1	288	2.8
ADM** [94]		30—35	3000—7000	0.5—1	100—150	3000—7000	1.0
TPC * [75]	Cylindrical multilayer drift chambers	0.8	192	0.4	10	14000	2.5
JADE [95]		0.6	48	1.0	4	1536	4.7
AFS [96]		0.6	42	0.8	1	3444	9.6
ARGUS * [97]		0.65	36	1 8	1	~6000	—
UA-1 * [98]		1.12	~ 100	Pressure of gas, atm	1	12200	6
HRS * [99]		0.7	47	1.5	2		4.5
CLEO * [100]	Cylindrical multilayer proportional chambers	0.8	117	0.7	2.4	28000	4.3
TASSO [101]	Cylindrical drift chambers + proportional chambers	0.8	15	1.2	1	2340	—
MARK-II [102]		1.14	16	1.2	1	3204	—
CELLO [103]		0.6	12	1.0	1		—

*In development stage.
**In design stage.

The number of layers in chambers used to identify hadrons reaches 200–300, the number of channels of the electronics varies in wide ranges, the layer thickness is $Pl = 1.6$–6 atm·cm, the length L of the flat proportional and drift chambers is 3–7.5 m, and the diameter of the cylindrical chambers is 1–2 m. In the last column, we give the values of the pulse-height resolution σ_n, which will be discussed below.

It is intended to make wide use of pictorial chambers in the new facilities planned for the LEP storage rings at CERN,[104-107] for the $\bar{p}, p$ storage facility at Batavia, and for the Large Accelerator and Storage Facility at Serpukhov.[92-94] We now consider some of the characteristic features of these types of multilayer chamber.

Multilayer proportional chambers. Two instruments of this type are in use: the multilayer proportional chamber EPI (External Particle Identifier), which is set up behind the bubble chamber BEBC at the SPS accelerator at CERN,[52,108] and the multilayer proportional chamber in operation in the PION facility,[89] which is intended for identification of cosmic rays (see Table VI).

As an example, we give the main parameters of the EPI chamber, which has total length $L = 7.7$ m (Fig. 13).

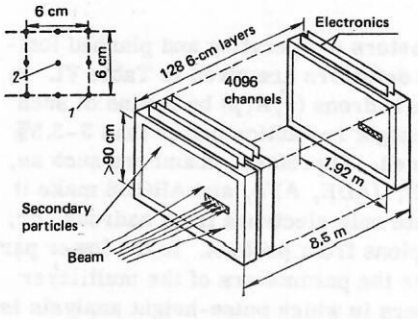

FIG. 13. Scheme of the multilayer proportional chamber EPI.[108]

It has 128 layers, each containing 32 proportional counters measuring 6 × 6 cm, at the center of which the sense wires are placed. The number of spectrometric channels of the electronics is 4096. Each channel consists of a preamplifier, an amplifier, an eight-bit analog-to-digital converter, and a buffer memory.

The advantage of multilayer proportional chambers compared with multilayer drift chambers is the simpler (and cheaper) electronics, the shorter dead time, and the smaller influence on the measured pulse height of various unfavorable factors that we shall discuss below. Among the shortcomings of the multilayer proportional chambers are the large number of channels of the electronics and the poor space resolution, which makes it difficult to use such chambers when there is a high multiplicity of charged particles in a narrow cone (jet).

Multilayer drift chambers. Flat chambers. At the present time, there are several identifiers of this type in operation: ISIS-1 at CERN,[90,109] CRISIS at Batavia,[91] and ISIS-2 under construction at CERN.[54] Other such chambers are at the model and design stage: ASTRON at the Institute of Theoretical and Experimental Physics,[92] IKS at the Joint Institute for Nuclear Research, Dubna,[93] and the argon neutrino detector (collaboration between the Institute of Theoretical and Experimental Physics, the Joint Institute for Nuclear Research, and the Moscow Engineering Physics Institute).[94]

The general form of a flat multilayer drift chamber is shown in Fig. 14. It is placed in a gas container with a volume up to several tens of cubic meters and contains a set of sense wires spanned in the center of the sensitive volume at right angles to the particle beam. The principle of operation of a flat detector of this kind is illustrated in Fig. 14a. It has a central frame with wires, which can be called a proportional chamber, and two large drift volumes on either side of it. The drift volumes are bounded by metallic plates, electrodes, to

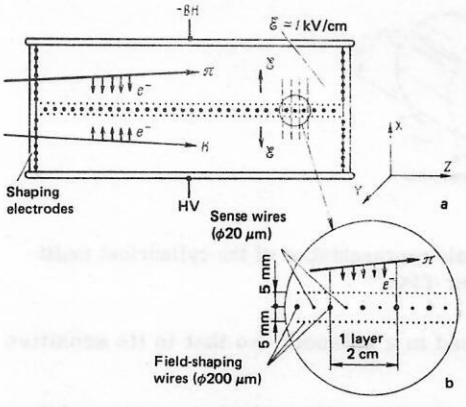

FIG. 14. Scheme of multilayer drift chamber (−HV signifies a negative high voltage) (a), and details of the central part of the chamber (b)

which a high constant voltage is applied (up to 200 kV in the ISIS chamber). Within the drift volumes, a uniform electric field is created. The uniformity of the field (better than 1%) is ensured by annular field-shaping electrodes, which bound the drift volumes on four sides and to which a linearly decreasing potential is applied. Under the influence of the electric field, the electrons produced along the tracks of the charged relativistic particles drift toward the central plane. The drift time of the electrons determines the X coordinate of the track. The Z coordinate along the beam is given by the number of the wire that responds. The Y coordinate can be determined, for example, by the current-division method (see below).

One of the possible constructions of the central part of the chamber is shown in Fig. 14b. It contains three planes of wires. In the central plane, sense wires (of diameter ~20 μm) alternate with thicker field-shaping wires (diameter 100–200 μm) separated by 4–5 mm. A voltage of several kilovolts is applied to the sense wires, which ensures the necessary gas amplification. At a distance of 4–5 mm on both sides of the central sense plane there are grids of wires of diameter 50–100 μm. They separate the drift volume from the proportional volume, in which electric fields of different intensity are produced, and ensure a high uniformity of the field in the drift volume. Simultaneously, positive ions drifting from the proportional region into the drift volume can be collected on these grids. This makes it possible to eliminate partly the field nonuniformity due to the accumulation of space charge and thus increase the useful load of the detector.

The choice of the geometry of the wires in the central plane of a multilayer drift chamber depends on many still inadequately studied factors, which we shall consider below. Usually, two neighboring sense wires forming a layer of thickness 1.5–2 cm are combined into one channel, into which the charge released in this layer is sent. In this way one can form 200–300 such layers along the chamber.

As an example, we give the size of the sensitive volume of the chamber ISIS-2: length 5 m, width 2 m, and height 4 m (2 m in each direction from the central plane). The length of the identifier and the number of layers are determined by the requirements on its pulse-height resolution (see Table VI). The gas container of the chamber (about 60 m^3) must be well sealed to maintain a constant composition of the gas. The rate of flushing of the gas is several tens of liters per minute, since the gas is exchanged only once in two days if the flushing rate is 20 liter/min and the volume is 60 m^3. In front of and behind the gas container there are windows covered by two layers of mylar.

Flat multilayer drift chambers contain a small amount of matter in the path of the particles, which means that there is little multiple scattering. For example, the ISIS-2 chamber has radiation length 0.07 and nuclear length 0.02.[90] The frames onto which the wires are wound are at right angles to the beam axis, so that the particles pass only through gas.

The advantage of multilayer drift chambers compared with the multilayer proportional chambers is the good space resolution and the capacity to distinguish closely spaced tracks (Table VII). The number of channels in the former is appreciably less than in the latter, although they are more complicated and, accordingly, more expensive. A shortcoming of multilayer drift chambers is their dead and memory time (for example, in the ISIS chamber electrons are collected from the volume of the chamber during a time of about 50 μsec). Serious technical problems are also associated with the use in such chambers of a high (up to 200 kV) constant voltage.

Cylindrical multilayer drift chambers. Chambers of this type, placed in a magnetic field, are used in colliding-beam experiments, and they have recently become a necessary part of many experimental facili-

TABLE VII. Space resoltuion of ionization identifiers (see text).

a) Multilayer proportional chambers and flat multilayer drift chambers

Detector		σ_x, mm	Method of determing the coordinate y across the field	σ_y, mm	ρ_2, mm
Multilayer proportional chamber	EPI	30	—	—	60
	PION	15	—	—	30
Flat multilayer drift chambers	ISIS	3	—	—	20
	CRISIS	—			20
	ASTRON	8	Electron drift time	$\leqslant 0.5$	$\geqslant 20$
	IKS	3	Current division	20	20
	ADN	0.15	The same	10	2

b) cylindrical multilayer drift chambers

Detector	Magnetic induction, T	$\sigma_{r\varphi}$, mm	Method of determining the z coordinate along the chamber axis	σ_z, mm	σ_p/p^2, %/GeV²	ρ_2, mm (deg)
TPC	1.5	0.1	Electron drift time	1—2	1.0	21
JADE	0.45	0.18	Current division	16	3.3	7
AFS	0.5	0.25	The same	17	2.5	4°
ARGUS	—	0.1	Additional planes of wires turned through a small angle	—	—	9
TASSO	0.5	$\geqslant 0.22$	The same	3—4	2.0	16
CLEO	0.5	0.25	The same	5	5.0	25
MARK-II	0.4	0.21	The same	4	1.9	1.4°—2.5°
UA-1	0.7	0.25	Current division	8—25	—	—
CELLO	1.3	0.21	Cathode read-out	0.4	1.5	3.5°

ties.[110] In what follows, we shall be concerned with cylindrical multilayer drift chambers, which are capable of identifying hadrons (π, K, p) on the basis of multiple measurement of the ionization. Such chambers are already used or being constructed at SLAC: TPC (Time Projection Chamber),[75] at DESY: JADE,[95] and at CERN: AFS.[96] Also in this category is the Central Detector of the UA-1 facility.[98] The main parameters of these chambers are given in Tables VI and VII.

There are various approaches to the construction of cylindrical multilayer drift chambers (see, for example, Refs. 2 and 111). At the present time, there are three main forms of such chambers:

1) With axial drift of the electrons (the TPC chamber). They are distinguished by the long drift length of the electrons ($L_d \approx 1$ m), the use of a high voltage (about 100 kV), and parallel electric and magnetic fields: $\mathscr{E} \parallel B$.

2) With azimuthal drift of the electrons (the chambers TASSO and AFS); these are of the *bicycle-wheel* type. They contain very many wires, and the electrons drift over short distances (less than 15 cm). In these chambers, one usually has $\mathscr{E} \perp B$ (Fig. 15).

3) With a cylindrical sensitive volume divided by wires into rectangular sections (UA-1 chamber). Such chambers consist of a set of flat multilayer drift chambers.

As an example, we consider a chamber of the first type: TPC (Fig. 16). It is placed around the position of intersection of the colliding electron and positron beams of the PEP accelerator and ensures detection of secondary charged particles under conditions of almost 4π geometry. The TPC chamber is a cylindrical vessel with a volume of several cubic meters filled with a working gas. In the bases of the cylinder there are multiwire proportional chambers of special configuration. A system of electrodes produces within the cylinder an axisymmetric electric field, in which the electrons, produced along the particle tracks, drift parallel to the cylinder axis on both sides of the center. The

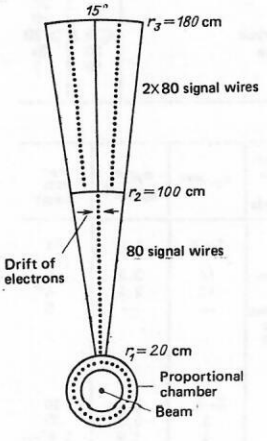

FIG. 15. Configuration of the wires in a section of a cylindrical multilayer drift chamber of the "bicycle wheel" type.[104]

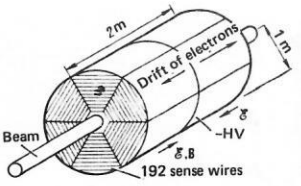

FIG. 16. Schematic representation of the cylindrical multilayer drift chamber TPC.[75]

chamber is placed in a solenoid, so that in its sensitive volume $\mathscr{E} \parallel B$.

The Z coordinates (along the cylinder axis) are determined from the time of flight of the electrons to accuracy $\Delta Z = \pm 0.2$ mm. Along the edges of the cylinder, the sense wires are arranged in the shape of concentric hexagons (see Fig. 16). Thus, the radius of the chamber is divided into 192 layers, in each of which the track coordinates of the particle and its energy loss are measured. The azimuthal angle φ with respect to the track is determined at 12 points by measuring the charge induced on the cathodes of the proportional chambers. This method makes it possible to determine the value of $r\varphi$ with rms error $\sigma_{r\varphi} = \pm 0.1$ mm,[112] where r is the distance from the measured point on the track to the chamber axis.

Cylindrical multilayer drift chambers have a large number of electronics channels (Table VI) and a complicated read-out system (see below). The need to place them in a magnetic field and surround them by electromagnetic and hadronic calorimeters imposes stringent limitations on their size. In turn, the need to identify particles over a fairly short length (about 1 m) makes it necessary to use a high pressure (up to 10 atm).

The main advantage of the cylindrical chambers is the possibility of detecting particles under conditions near 4π geometry. These detectors permit complete reconstruction of events with high multiplicity and the identification of secondary particles.

Factors determining the reliability of particle identification

Number and thickness of layers. The length of a multilayer identifier is usually determined by the geometry of the experimental facility, and also by technological and economic considerations. In choosing the optimal number of layers in the chamber, it is necessary to take into account the following factors:

1) with increasing number of layers, the pulse-height resolution improves comparatively slowly;

2) the main part of the cost of the instrument (60–75%) is due to the electronics, so that an increase in the number of channels is undesirable;

3) the pulse height and the signal-to-noise ratio depend on the thickness of the gas layer and on the configuration in which the wires are arranged;

4) with increasing pressure, the effective thickness of a layer increases linearly, but the relativistic rise in

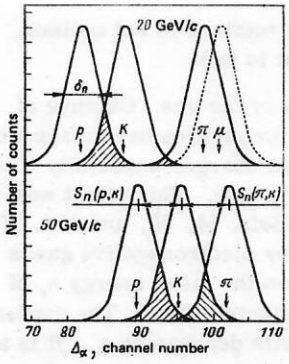

FIG. 17. Calculated distribution of the Δ_α values obtained by the truncation method for $p = 20$ and 50 GeV/c for Ar + 5% CH_4 mixture in the 128-layer EPI detector, $\sigma_n = 2.5\%$.[53]

the ionization energy loss decreases;

5) with increasing thickness of a layer, the pulse-height resolution of the instrument improves but the space resolution deteriorates.

To compare different identifiers, it is convenient to introduce the separation coefficient S_n, which determines the reliability of identification of particles, for example, π and K mesons, in units of the standard deviation σ_n:

$$S_n(\pi, K) = 2.355\, D(\pi, K)/\delta_n = [\Delta_0(\pi) - \Delta_0(K)]/[\Delta_0(\pi)\cdot\sigma_n]. \quad (29)$$

This definition of S_n is possible because, as was shown above, the distribution of the Δ_0 (or Δ_α) values measured in an identifier with n layers is Gaussian. For example, if the instrument resolution is $\sigma_n = 2.5\%$ and $p = 20$ GeV/c, then $S_n(\pi,K) \approx 5.5$, $S_n(p,K) \approx 3$, and $S_n(\pi,p) \approx 9$ (Fig. 17).

Similarly, for one layer

$$S_1(\pi, K) = 2.355\, D(\pi, K)/\delta(\pi) = 2.355\,[\Delta_0(\pi) - \Delta_0(K)]/\delta(\pi). \quad (30)$$

If the truncation method with $\alpha = 0.4$ is used, then for S_n and S_1 we have[63]

$$S_n(\sigma_n) = n^{0.428} S_1(W), \quad (31)$$

and, for example, the transition from $n = 1$ to 200 improves the reliability of identification of the particles by about 10 times.

If we assume that it is reasonable to pay for an improvement in the separation coefficient S_n by 10% by a doubling in the number of channels of the electronics, then the optimal layer thickness Pl is about 5 atm·cm for Ar, 3 atm·cm for Xe, and 2 atm·cm for propane. From this point of view the chambers EPI ($l = 6$ cm, $P = 1$ atm), JADE ($l = 1$ cm, $P = 4$ atm), and TPC ($l = 0.4$ cm, $P = 10$ atm) have correctly chosen layer thickness, whereas in the ISIS chamber the layers are too thin ($l = 1.6$ cm, $P = 1$ atm) and the number of layers too great ($n = 320$). All the listed chambers operate with a mixture of argon and carbon dioxide gas or methane.

The separation coefficient $S_n(\pi,K)$ in a chamber of length $L = 128.8$ cm is shown as a function of the gas

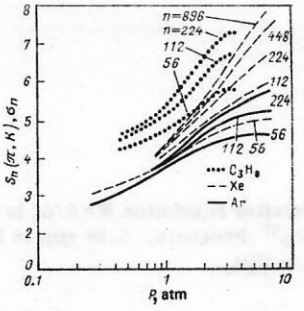

FIG. 18. Dependence of the separation $S_n(\pi, K)$ of π and K mesons with momentum 3.5 GeV/c on the pressure in a proportional chamber of length $L = 128.8$ cm divided into n layers.[63]

pressure (Ar, Xe, and C_3H_8) in Fig. 18. It can be seen that the division of the chamber into a set of thin layers does not significantly improve its resolution. It can be seen that for a small number of layers it is best to use propane. On the other hand, if a high resolution is needed, it is necessary to use Xe at high pressure and increase the number of layers.

These considerations make it possible to optimize the number and thickness of the layers for given length and resolution W_n (%) of the instrument. Curves calculated by the method of maximal likelihood that enable one to choose the thickness and number of layers for Ar at atmospheric pressure are shown in Fig. 19. These calculations did not take into account the spread of the gas gains on the wires and charge exchange between channels. The minimal instrument length for given resolution W_n is obtained at a layer thickness of $l \approx 3$ cm. A large number of layers does not give advantages justifying the increased cost of the chamber. It is more advantageous to increase, not the number of layers, but the length of the chamber and the gas pressure. A large number of very thin layers in a chamber were used, for example, by Ludlam *et al.*[113]

Composition of the gas. The gas mixture must ensure: 1) a large relativistic rise of the ionization energy loss; 2) good pulse-height resolution; 3) that the electron drift velocity is independent of the voltage; 4) a low cost of filling the chamber; 5) that there is no danger of an explosion.

The largest relativistic rise of the ionization energy loss occurs in heavy noble gases (see Table III). How-

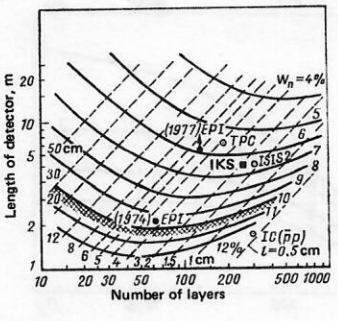

FIG. 19. Optimal number n and thickness l (cm) of layers for given length L and given pulse-height resolution W_n (%) of a multilayer identifier.[108]

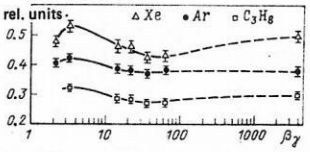

FIG. 20. Dependence of the relative resolution $W = \delta/\Delta_0$ in a layer of thickness 2.3 cm on $\beta\gamma$.[63] Pressure: 5.84 atm in Xe, 7.13 atm in Ar, and 3.13 atm in C_3H_8.

ever, a serious obstacle to the use of Xe and Kr is their high cost. The approximate ratios between the costs of the noble gases is Ar:He:Kr:Xe ≈ 1:2:35:170.

The relative pulse-height resolution W of a single-layer detector ($l = 2.3$ cm) as a function of $\beta\gamma$ is shown in Fig. 20. The curves for the different gases also correspond to different pressures. Since W is virtually independent of the velocity of the particle, the shape of these curves is determined by the change in Δ_0. We emphasize once more that the relative resolution is better in multiatomic gases than in noble gases (see above). Although the relativistic rise decreases with increasing pressure (Fig. 21), the separate identification of particles improves because of the increase in the resolution until the onset of saturation due to polarization effects in the gas (see Fig. 18). The best resolution is attained in propane at a pressure of 2–3 atm. It should be noted that the questions associated with the optimal choice of the gas and its pressure have not yet been adequately studied, and at the present time such investigations are being made in many laboratories.[106,112] In practice, because of its low cost, Ar is used in almost all experiments, about 10–20% carbon dioxide gas or methane being added to it usually. This mixture is not optimal, but it is cheap and convenient in use.

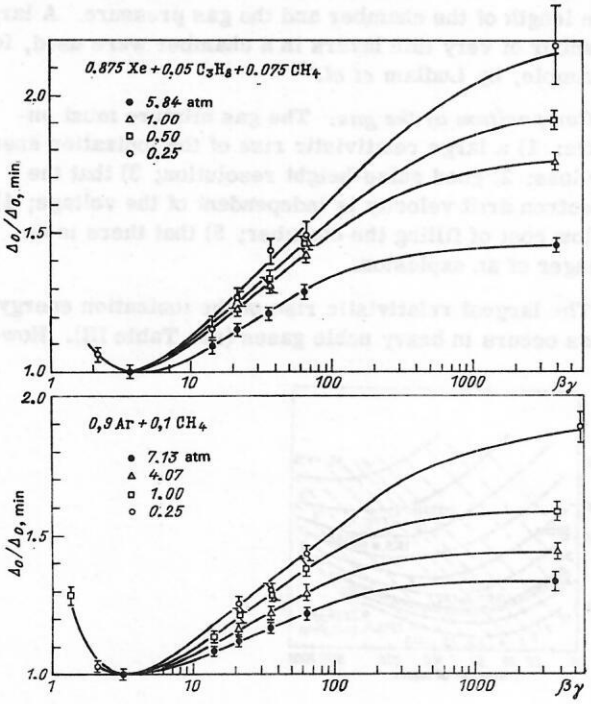

FIG. 21. Dependence of the relative growth of the probable energy loss in xenon and argon on $\beta\gamma$ at different gas pressures, $l = 2.3$ cm.[63]

Requirements on the purity of the gas. Capture of electrons by electronegative impurities has an appreciable influence on the collected charge, especially if the drift length of the electrons is long. This effect was investigated, for example, in Refs. 54, 90, and 114. The rate of capture of electrons by electronegative gases (above all, oxygen) depends on the mean energy ε_e of the electrons moving in the electric field. The capture coefficient $k_e(\varepsilon_e)$ increases with decreasing ε_e. It is assumed that in the capture process a catalyst participates, the role of the catalyst being played by the quenching gas (CO_2, CH_4) present in the mixture. The lifetime τ_e of free electrons in a gas with oxygen (water) concentration α_1 and concentration α_2 of the quenching gas is

$$\tau_e = 1/[k_e(\varepsilon_e)\,\alpha_1\alpha_2]. \qquad (32)$$

In a "sufficiently pure" gas the lifetime of free electrons with near-thermal energy ε_e is about 100 μsec.[114] At higher values of ε_e, the electron lifetime increases by more than an order of magnitude. The dependence $k_e(\varepsilon_e)$ is rather complicated and needs to be determined more accurately.

Carbon dioxide gas catalyses capture of electrons at the rate

$$\nu_e = (3.1 \pm 0.3)10^{-30}\alpha_1\alpha_2\ [\text{sec}^{-1}], \qquad (33)$$

where α_1 and α_2 can be expressed in terms of the number of molecules in 1 cm^3.[115]

For oxygen volume concentration $\alpha_1 = 2\times10^{-6}$ and carbon dioxide gas concentration $\alpha_2 = 0.2$, the lifetime of free electrons is $\tau_e \approx 1.4$ msec. If the drift velocity of the electrons in the chamber is $v_d = 2$–3 cm/μsec, the mean range until absorption is $L_a \approx 30$ m, and if the volume concentration of the oxygen is $(1$–$2)\times10^{-6}$ the electrons can drift over a length of 1–2 m without appreciable loss. For $\alpha_1 = (8$–$10)\times10^{-5}$, $\tau_e \approx 35$ μsec,[54] which agrees well with the calculations.

The influence of electron capture in the case of a large drift length L_d on the pulse height was investigated in Ref. 90. For $\alpha_1 = 2\times10^{-6}$, $L_d = 2$ m, and $\varepsilon = 60$ kV/m, the pulse height decreases by about 17%. Such a decrease seriously hinders identification of the particles. This effect can be greatly reduced by improving the purity of the gas and raising the drift voltage and the drift velocity. It is obvious that in the design of ionization particle identifiers great attention must be paid to electron capture in the gas.

Gas pressure and the admissible range of particle momenta. We estimate the range of momenta in which particles can be effectively identified by measurement of the ionization. This range depends on the relativistic rise of the ionization energy loss in the gas and on the pulse-height resolution of the instrument. The lower limit is determined by the ionization minimum, which for π and K mesons and protons is in the range of momenta 0.5–4 GeV/c. The dependence of the separation coefficient S_n on the particle momentum in a chamber

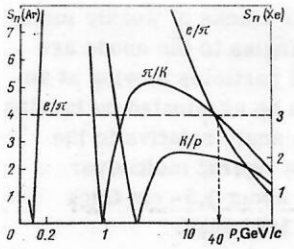

FIG. 22. Dependence of the separation coefficient S_n (in units of σ_n) on the particle momenta in Ar ($P=4$ atm) and Xe ($P=1$ atm); $L=1.7$ m, $n=170$.[104]

with $L=1.7$ m filled with argon at $P=4$ atm is shown in Fig. 22.[104] For comparison, we give the dependence S_n in the same chamber filled with xenon at $P=1$ atm. It can be seen that π and K mesons can be effectively separated in the range of momenta 2–40 GeV/c. It is possible to separate p and K in the interval 5–40 GeV/c with a reliability that is not high.

The upper limit of the momentum at which effective particle identification is attained is due to saturation of the relativistic rise of the ionization—the Fermi plateau—and increases with decreasing pressure of the gas. Effective separation of high-energy particles can be achieved only in a detector of considerable length at atmospheric or reduced pressures. We shall assume that the particle identification is satisfactory, provided $S_n \geq S_n^0/\sqrt{2}$. (We denote the maximal value of the separation coefficient by S_n^0, and the maximal particle momentum corresponding to this condition by p_M.) The dependence of p_M on the pressure in different gases is shown in Fig. 23. At a pressure of 1 atm, p_M is 75 in xenon, 30 in argon, and 15 GeV/c in propane. For the identification of secondary particles with momenta 3–15 GeV/c, multiatomic gases, for example, propane or isobutane, at pressure 1–3 atm, are the most suitable. At the same time, argon is the most universal and, therefore, convenient filler for particle identifiers in the momentum range 3–30 GeV/c. Secondary particles with $p \approx 100$ GeV/c can be identified in xenon at a reduced pressure. We recall that drift chambers also work reasonably when $P<1$ atm.[116,117]

It is well known that the mean multiplicity N_{ch} of secondary charged particles produced on a fixed target at a beam energy of several TeV is $N_{ch} \geq 10$. In the antiproton–proton storage rings at CERN (energy 2×270 GeV), $N_{ch} \approx 50$.[118] Thus, the majority of secondary particles will have momentum 150 GeV/c, and they can be successfully identified by multiple measurement of the ionization.

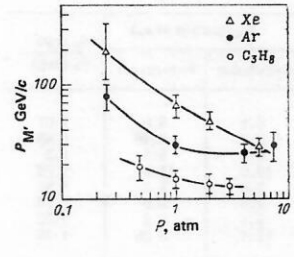

FIG. 23. Dependence of the maximal momentum p_M for identification of π and K mesons on the gas pressure ($l=2.3$ cm).[63]

Charge exchange between channels. In a multilayer drift chamber, there are correlations between the pulse heights in neighboring channels. Such correlations are due, not to delta electrons (this effect is small and can be ignored[59]), but primarily to the diffusion of electrons from the neighboring layers, especially when there is a large drift length. The charge collected in layer i is

$$Q_i = M_i [(1-2a)\, q_i + a q_{i+1} + a q_{i-1}], \tag{34}$$

where q_{i-1}, q_i, q_{i+1} are the charges in channels $i-1$, i, and $i+1$, respectively, M_i is the gas gain in channel i, and a is a correlation coefficient, which depends on the electron drift length in each layer. Thus, for a 75-cm drift length, $a=0.1$.[90] Such charge exchange is positive, and it has little influence on the pulse-height resolution of the instrument.

Another type of charge exchange—negative—arises as the signal is passed from the chamber to the channels of the electronics. It is due to capacitive coupling in the channel circuits and is characterized by a correlation parameter α_c. The upshot is that the charge in channel i is

$$Q_i' = \alpha_c Q_{i-1} + Q_i + \alpha_c Q_{i+1}. \tag{35}$$

According to calculations by the Monte Carlo method for the ISIS chamber, $\alpha_c = -0.055 \pm 0.01$.[59] The minus sign means that the charge exchange between the channels displaces the spectra of the ionization energy loss to smaller amplitudes.

The capacitive coupling between a plane of sense wires and the high-voltage electrodes can have a more significant influence on the resolution, giving rise to a displacement of the zero point that is proportional to the pulse height. This effect is characterized by a parameter b_c, so that (35) becomes

$$Q_i' = \alpha_c Q_{i-1} + Q_i + \alpha_c Q_{i+1} - b_c \Delta_0. \tag{36}$$

For the ISIS chamber, $b_c = 0.20 \pm 0.04$. Capacitive coupling can become the reason for systematic error in the analysis of data. This effect can be eliminated by: 1) decreasing the capacitance between the high-voltage electrodes and the plane of the sense wires; 2) introducing a shunting capacitance to the high-voltage electrodes.

Gas amplification. The requirements on the accuracy of preparation of the details of a multilayer drift chamber are basically the same as for "ordinary" drift chambers. Additional requirements arise from the need to produce the same conditions for measurement of the charge at a large number of sense wires. The main reasons for the spread of the gas gain at individual sense wires are given in Table VIII.

Fluctuations of the pressure and temperature have a strong influence on the operation of large multilayer chambers. The pulse-height variations during 3.5 days in the EPI chamber are shown in Fig. 24.[61] There is an

TABLE VIII. Reasons for the spread of the gas gain at individual wires.[59]

Parameter	Limits of variation of the parameter	ΔM, %
Instability and pulsations of the drift voltage	$<10^{-3}$	<0.7
Instability and pulsations of the anode voltage	$<10^{-4}$	<0.1
Instability of the voltage supplying the electronics	$<10^{-2}$	<1
Variations of M in time associated with variations in the temperature, pressure, composition of the gas mixture, etc.	$1.6\cdot10^{-2}$	<2
Variation of M along a wire	$\leqslant 2\cdot10^{-2}$	<2
Differences between M on individual wires associated with spread of:		
the diameters of the wires	<0.2 μm	—
the distance between the sense wires	<8 μm	—
the distance between the potential wires	30 μm	~ 2
the positions of the field-shaping electrodes	40 μm	~ 2
Noise in the electronics	120 eV/channel	1

obvious inverse correlation between the pressure and the pulse height. When the pressure is increased by 1%, the pulse height decreases by (6.5 ± 0.5)%. When the pressure increases, the value of $\mathscr{E}/P$ near a sense wire decreases and the gas amplification is reduced. The fluctuations in time of the pulse height are so appreciable that without a good monitor and the introduction of corresponding corrections particle identification is impossible.

In large multilayer chambers with vertically arranged sense wires the gas gain may depend on the temperature gradient. The influence of this effect has not yet been studied.

In the process of gas amplification, a large number of positive ions arises near the sense wire. They drift in the opposite direction with velocity approximately 10^3 times less than the electrons. The accumulation of the positive space charge leads to: 1) a decrease in the gas gain near the sense wire; 2) a change in the velocity and direction of motion of the electrons in the drift volume.

Electrons from the tracks of particles moving at right angles to a sense wire are collected on it at effectively a single point, where a high charge density is formed during the gas amplification process. The positive charge "screens" the wire and thus effectively reduces the field intensity around it. This is confirmed experimentally: For strongly ionizing particles a decrease in the pulse height by 10% compared with the case when the track is parallel to the wire was already noted for $M=10$.[119] According to the data of Ref. 120, when M

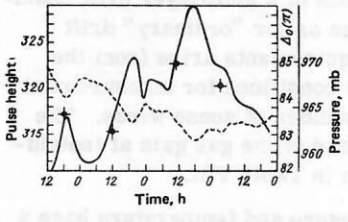

FIG. 24. Correlation between the pulse height in the ISIS chamber and the variation of the atmospheric pressure.[61] The continuous curve is the pulse height from a radioactive source, and the broken curve shows the atmospheric pressure.

$=10^4$ the pulse heights from the tracks of weakly ionizing particles moving at right angles to the anode are 25% smaller than for the same particles moving at angle 45°. This shortcoming can be eliminated by turning the chamber through a certain angle relative to the axis of the particle beam. In a typical multilayer drift chamber with each layer about 1.5- cm thick this angle for $M=10^4$ is about 100 mrad.

The gas amplification in the chamber also depends on the electron drift length. A bunch of electrons expands over the drift path by diffusion, and the extended bunch is multiplied more effectively near a wire. Charpak *et al.*[121] observed that the pulse height increases by 10% if a source (^{55}Fe) situated in the immediate proximity of the sense wires is displaced through a distance of 15 cm. In an investigation of the dependence of the change in the gas amplification on the load,[122] it was established that in a chamber with volume $1\times1\times1$ m the value of M decreases by about 10% when the load is increased to 2×10^2 cm$^{-2}\cdot$ sec^{-1}. This last value corresponds to the condition of effective collection of positive ions on the grid between the proportional and drift volumes.

It follows from what we have said above that it is necessary to use minimal gas amplification and effective collection of positive ions in the chamber.

In conclusion, we note that the effects that influence the pulse height must be taken into account in the data analysis. The experimental values of the pulse-height resolution in different chambers are compared with the calculated values in Table IX. It can be seen that there is a large discrepancy between the results of the calculations and the experiments. A resolution close to the calculated value was achieved only in the identifer ISIS-1, in which the electrons in each layer are collected on one sense wire, and the pulses from it are analyzed in one channel of the electronics. In addition, in operation with this chamber particular attention was paid to the composition and purity of the gas, to the analysis of the pulses, and to the calibration. Before the start of measurements, it is important to make a careful calibration of the instrument and a series of methodological investigations. During the collection of data, it is necessary to check the conditions of operation of the identifier regularly.

TABLE IX. Comparison of calculated and experimental values of the particle separation coefficient $S_n(\sigma_n)$ for different identifiers.[105]

Identifier	Separation of particles	p, GeV/c	S_n (in units of σ_n)		$\frac{S_n\text{ (cal)}}{S_n\text{ (exp)}}$
			Calculation	Experiment	
ISIS-1 *	e/π	0.5	8.1	8.0	1.01
CRISIS *	π/p	40	3.2	2.16	1.48
EPI	π/p	50	6.1	5.1	1.2
TPC*	e/π	0.8	18.0	11.8	1.36
JADE(JET)	e/π	0.45	7.8	4.2	1.86
JADE	e/π	0.45	7.8	5.0	1.56
HRS	e/π	4	4.1	3.2	1.32
CLEO	e/π	0.45	11.1	8.25	1.36

*Prototype

Space and time resolution of multilayer detectors

Space resolution of large drift chambers. The space resolution of multilayer proportional chambers is determined by the distance between the wires (for example, 6 cm in the chamber EPI). Therefore, improvement of the resolution in these chambers directly involves an increase in the cost of the instrument.

In multilayer drift chambers, one can achieve good space resolution, this being determined by: a) the statistical fluctuations in the formation of the primary bunches of electrons—the clusters on the particle track; b) the time resolution of the electronics; c) diffusion of the electrons. Factors a) and b), which determine the space resolution for a short drift length L_d of the electrons, are analyzed in Refs. 10, 107, and 123–126. In multilayer drift chambers with large L_d (ISIS, TPC, IKS) the rms error σ_x in the finding of the coordinate X along the drift direction of the electrons is completely determined by the spreading of the electron cloud due to diffusion. The diffusion of the electrons depends on their mean energy $\varepsilon_e = kT_e$, where T_e is the temperature of the electron gas, and k is Boltzmann's constant. The spreading of the point charge during drift over the length L_d in an electric field with intensity $\mathscr{E}$ is characterized by the rms deviation of the electrons within the cloud:

$$\sigma_d = [2L_d k T_e/(e\mathscr{E})]^{1/2}. \tag{37}$$

Allison *et al.*[90] found that $\sigma_d = 2$ mm for $L_d = 1$ m in an Ar + 20% CO_2 mixture.

In several studies on drift chambers[116,117,125] it has been shown that in the saturation region of the drift velocity the space resolution is almost two times better than predicted by the relation (37). Sauli[123] explains this effect by the fact the diffusion in the drift direction is appreciably less than in the transverse direction. As a result, the cloud of electrons does not have a spherical shape after a long drift but acquires a disk shape. It follows that if there is a sufficiently high voltage across a drift gap of length 1 m, a resolution of $\sigma_x \approx \pm 1$ mm can be achieved.

The values of σ_x and $\sigma_{r\varphi}$ characterizing the space resolution of a multilayer drift chamber are given in Table VII. For such chambers with large drift length of the electrons the upper limit of σ_x is given. Such resolution is achieved for tracks maximally far from the plane of the sense wires. Closer to it and when $L_d \leq 20$–50 cm the time resolution of the electronics determines the $\sigma_x < 1$ mm. The space resolution $\sigma_{r\varphi}$ of the cylindrical multilayer drift chambers in Table VII corresponds to the best resolution achieved in these chambers for small L_d.

An important characteristic of multilayer drift chambers is the two-track resolution ρ_2. The physical meaning of ρ_2 is that two tracks in a given layer of the chamber passing through an area $\rho_2 L_w$ cannot be resolved (L_w is the length of the sense wire). In "ordinary" drift or proportional chambers, ρ_2 is determined by the distance between the sense wires. In pictorial chambers, it is characterized by the pulse duration and the capacity of the electronics to analyze pulses that follow one another rapidly. The two-track resolution ρ_2 achieved in large multilayer proportional and drift chambers is given in Table VII.

The coordinates along a sense wire of length L_w can be measured by:

1) The current-division method; the method has been well studied[127–129] and is frequently used (see Table VII). The space resolution is limited by the signal-to-noise ratio, so that $\Delta L_w / L_w \approx 1\%$.

2) Measurement of the centroid of the pulses induced on the cathode planes[130–132]; the method ensures a high space resolution $\Delta L_w \approx 0.1$ mm. However, it can be used when the sense wires are arranged along the edges of the chamber as, for example, in the TPC chamber[112].

3) Using as cathode a delay line,[117,133] measurement of pulse arrival times from the two ends of the delay line by means of special electronics.[134] In drift chambers, fast delay lines ensuring $\Delta L_w \approx 5$ mm for length 1–1.5 m of the delay line are used.

4) Planes of wires turned through a small spatial angle α_s (Refs. 101 and 102) relative to the main planes, which gives $\Delta L_w \approx 4$–5 mm (see Table VII).

5) Sense wires set up along the direction of motion of the particles[92]; the method ensures a space resolution equal to the distance between the wires ($\Delta L_w = 15$ mm in the chamber ASTRON).

The right–left ambiguity in multilayer drift chambers can be eliminated by displacing the wires from the sense plane (in the chamber JADE by 0.15 mm, in AFS by 0.4 mm) or by measuring the induced charge in grids near the sense wires.[93]

Influence of space charge. In the process of gas amplification near a sense wire the number of positive ions formed per unit time is

$$N_i = \int_0^{L_d^{\max}} M \frac{(-dE/dx)_{T_e}}{w} \exp(-L_d/L_a)\, d(L_d), \tag{38}$$

and these ions move slowly in the drift volume. In large chambers ($L_d^{\max} \geq 1$ m), their drift time τ_i is a fraction of a second. Thus, positive space charge accumulates in the drift volume. In the volume V, the charge density is

$$\rho_c = eN_i \eta_m \tau_i / V, \tag{39}$$

where η_m is the efficiency of penetration of ions from the proportional volume to the drift volume. The accumulation of space charge with density ρ_c in the thin layer Δx leads to a decrease in the electric field $\Delta\mathscr{E}$ in the direction of the normal to the layer Δx:

$$\Delta\mathscr{E} = (\rho_c/\varepsilon)\, \Delta x, \tag{40}$$

where ε is the permittivity. This change influences the velocity and direction of the drift of the electrons, and in the reconstruction of the event deformations of the track arise. Thus, in a multilayer drift chamber[122] filled with 80% argon and 20% methane and under the

conditions $\mathscr{E}/P = 1.5$ kV·cm^{-1}·atm^{-1}, ion mobility $\mu^+ \approx 1.9 \times 10^{-4}$ m^2·V^{-1}·sec^{-1}, $L_d^{max} = 1$ m, $M = 1.6 \times 10^3$, particle flux 10^5 sec^{-1}, $\eta_m = 0.08$, $N_i = 9.6 \times 10^4$ ion·cm^{-1}·atm^{-1} the charge density is $\rho_c = 40$ nC/m^3 and the change in the electric field is $\Delta\mathscr{E} = 50$ V/cm or $\Delta\mathscr{E}/\mathscr{E} = 3\%$, which leads to a small deformation of the image.

In the ISIS chamber, in which a grid for collecting positive ions is not used ($\eta_m = 1$), the admissible value is $\rho_c = 5$ nC/m^3, which corresponds to a particle flux density of not more than 1.3×10^3 m^{-2}·sec^{-1}. To reduce the dead time, the anode voltage is applied only during 5% of the time, during the time of operation of the bubble chamber situated in front of ISIS. This makes it possible to increase the load to 2.5×10^4 particles·m^{-2}·sec^{-1}, the quality of the image remaining good.

The dead time of large multilayer drift chambers. Multilayer drift chambers with large drift volume are slow instruments. Thus, in such a chamber with drift length $L_d = 2$ m the electron collection time is $\tau_{de} \approx 50$ μsec. This means that one can work in beams with a maximal intensity of about 10^4 particles·m^{-2}·sec^{-1}. If a multilayer drift chamber is used to identify charged particles after bubble chambers (ISIS, CRISIS, EPI), such a restriction on the load is not critical. The requirements on the dead time of cylindrical drift chambers are determined by the cycle duration of the storage ring.

Particle identifiers used in conjunction with electronic facilities (ASTRON, IKS) must operate under high loads. The problem of increasing the useful load of a large multilayer drift chamber reduces above all to decreasing the positive space charge density in its volume. We mention some ways in which this can be achieved: 1) by using screening grids to collect the positive ions ($\eta_m = 0.1$); 2) by creating an insensitive zone in the position through which the beam particles pass ($\eta_b = 0.1$); 3) by using a pulsed anode voltage (decrease in ρ_c by 2–10 times); 4) by reducing the gas amplification (decrease in ρ_c by 2–5 times); 5) by dividing the chamber into small sections (decrease of τ_{de}, τ_i, and ρ_c); 6) by using additional coordinate detectors before and after the identifier (an increase in the load by 2–10 times).

We consider these measures in more detail.

1. We have already discussed the introduction of screening grids between the proportional and drift volumes (see Fig. 17b). The use of such grids makes it possible to collect about 90% of the positive ions that reach the chamber from the sense wires.[122]

2. One of the variants for producing an insensitive region for beam particles used in the EPI (see Fig. 13) is based on covering part of the sense wire at the position where the beam passes by a thin film of glass. For a multilayer drift chamber one can use a different method. A metallic foil with width corresponding to the beam dimensions is attached to the screening grid at the point at which the beam passes along the chamber.[93] The electrons from the tracks of the primary particles drift toward the center of the chamber, where they are collected on the foil. Thus, the ionization produced by the beam particles does not contribute to the accumulation of the space charge in the chamber.

3. From the point of view of reducing the charge density, there is a large gain from pulsing the anode voltage. As will be shown below, the main restriction on the rate of accumulation of statistics is imposed by the time required to transfer information to the computer, which has the consequence that the rate of data collection does not exceed 100 sec^{-1}. Switching off the anode voltage during the analysis and transfer of information reduces the accumulation of the positive ions in the chamber by more than an order of magnitude.

4. The gas amplification cannot be reduced very strongly without influencing the accuracy of the measurement of the pulse height. However, it is desirable to work with a small gas amplification.

5. The division of a multilayer drift chamber into several smaller sections permits a significant improvement of its parameters. There is a reduction in the drift time, the space charge density, and the voltage on the electrodes, and there is an improvement in the space resolution. However, this is achieved by increasing the number of channels of the electronics and the cost.

6. The use of additional coordinate detectors (proportional or drift chambers) before and after the identifier makes it possible to eliminate during the analysis background and "old" tracks not associated with the studied event, simplifies the process of recognition of tracks, and, ultimately, shortens the dead time of the instrument.

The introduction of the listed improvements in multilayer drift chambers can significantly increase their useful load (by about two orders of magnitude).

Read-out and analysis of information in multilayer detectors

Read-out and analysis of information in multiwire drift chambers. The electronics for multilayer drift chambers must satisfy stringent requirements. Each sense wire sends a "batch" of signals, the number corresponding to the number of tracks in the chamber. The electronics is capable of storing and analyzing a limited number of pulses per event (in ISIS, up to 30), the minimal interval between them being 100-200 nsec.[135] The accuracy in the measurement of the charge must be about 1%, and the input sensitivity of the preamplifier not worse than 2 μA.

The task of the electronics is to measure the charge (the pulse height) and the arrival time of each pulse in the "batch." For this, it is necessary to amplify, store, and convert all signals, and also to transmit information to the buffer memory or directly to the computer. The structural scheme of the read-out system in the multilayer drift chamber IKS is shown in Fig. 25.[93]

The information from multilayer drift chambers can be analyzed in different ways. During the time of accumulation of information the pulses can be stored in analog

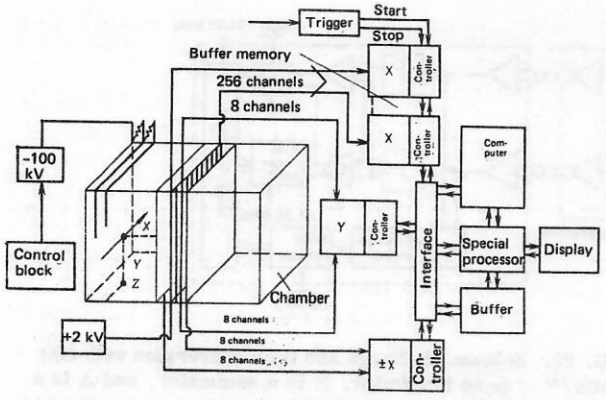

FIG. 25. Electronics for read-out from a multilayer drift chamber.[93]

form and then digitized relatively slowly. Another way is to use fast analog-to-digital converters (ADCs) with conversion time ≤100 nsec. Let us dwell in more detail on some typical variants of the electronics.

Information storage in a multiwire drift chamber in an analog memory. Analog memory using capacitors. The block diagram of charge and time conversion from an analog memory in a chain of capacitors is shown in Fig. 26. This type of electronics was used, for example, in the multilayer drift chambers ISIS,[135] CRISIS,[91] and JADE.[136] The pulses received from the sense wire are amplified in the preamplifier, which is in the immediate proximity of the chamber. The preamplifier must be fast and have low noise, have a low input impedance, and have stable amplification.

The main task of the electronics—the measurement of the charge and the arrival time of the pulses—is realized by the charge and time conversion block (Fig. 26). In the ISIS chamber, the pulses from the preamplifier are passed to the amplifier, where there is a

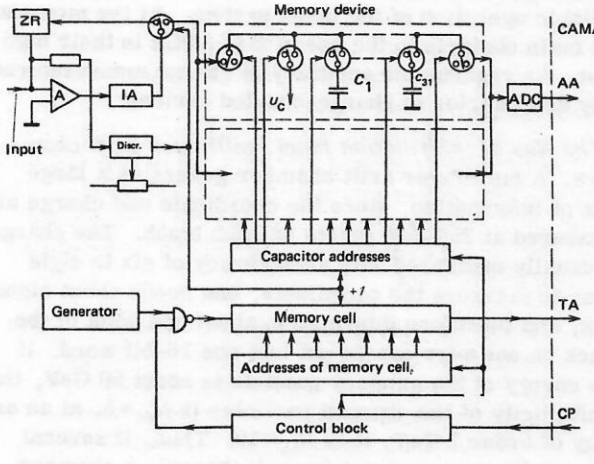

FIG. 26. Scheme of charge and time conversion with analog memory using capacitors.[93] A is an amplifier, ZR is the zero restorer, IA is the integrator–amplifier, AA is the pulse-height analysis, TA is the time analysis, CP is a control pulse, and U_C is the control voltage.

zero restorer, which makes it possible to pass a series of rapidly arriving pulses without distortion of their amplitudes. After amplification, the pulses are integrated and sent to the analog memory, which consists of 30 successive capacitors C_i, in each of which charge is stored.

An external trigger produces the pulse START, which activates the address register of the RAM and begins the measurement of the drift time of the electrons. When the pulse reaches the input of the charge and time converter, the pulse TREK is formed in the discriminator. This pulse is used to measure the drift time, since it is recorded at the appropriate address in the RAM buffer memory. The pulse TREK is also sent to the capacitor address register and opens the switch of the corresponding capacitor which stores a voltage corresponding to the charge in the pulse. Then the capacitor address is increased by unity, and the system awaits the arrival of the next pulse.

After completion of information acquisition from the chamber, the potential of each capacitor is steadily digitized by one relatively slow ADC (with conversion frequency 10–100 kHz). Simultaneously, the time information is read out from the RAM buffer memory, and all information about the pulse height and the drift time is analyzed further.

Analog memory using charge-coupled devices. A better analog memory can be created on the basis of charge-coupled devices (CCDs). Their principle of operation has been explained in several review papers (see, for example, Ref. 137) and the monographs of Refs. 138 and 139. An analog shift register, a line of charge-coupled devices, fulfills the same function as the chain of capacitors. The advantage of the charge-coupled devices is the high degree of integration and reproducibility of the properties of each element of the chain. This reduces the work of construction and adjustment and increases the reliability of operation of the electronics. Analog shift registers based on charge-coupled devices can be used in two variants: in the regime of continuous recording and in the regime of triggered recording.

An analog memory based on charge-coupled devices in the regime of continuous recording is used, for example, to analyze information from the multilayer drift chamber TPC.[140] The scheme of charge and time conversion based on charge-coupled devices is shown in Fig. 27. After the appearance of the pulse START from the external trigger, continuous read-out from the chamber commences (in the chamber TPC, with frequency $f_1 = 13$ MHz), and it is stored in the charge-coupled devices. At this rate of storing, the pulse is accommodated in six or seven cells of the charge-coupled devices. The necessary number of cells of the line of charge-coupled devices, $n_b = \tau_{de} f_1$, is determined by the time of complete collection of electrons in the chamber, τ_{de}, and the storing frequency f_1. For example, in a chamber with drift length 1 m, $\tau_{de} \approx 30$ μsec, and $f_1 = 10$ MHz, we have $n_b = 300$. It should be noted that this frequency of storing in the charge-coupled devices does not satisfy the requirements on the accuracy

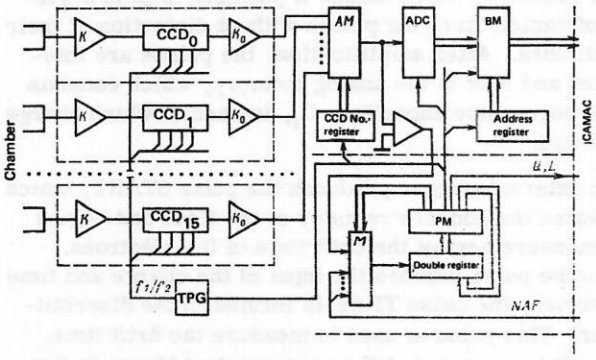

FIG. 27. Scheme of charge and time conversion with analog memory based on charge-coupled devices with continous recording.[93] K and K_0 are amplifiers, TPG is a time pulse generator, AM is an analog multiplexer, M is a multiplexer, BM is a buffer memory, PM is a programmable memory, and Q, L, and NAF are CAMAC commands.

of measurement of the pulse arrival time. It is necessary either to increase the storing frequency f_1 or to measure the pulse arrival time separately. It is also possible to fix the time by the peak of the pulse, found by calculating the centroid of the charge.[141]

After the collection of information has been completed, the frequency is reduced to $f_2 = 10$–100 kHz and the read-out from the charge-coupled devices commences. One standard ADC, in conjunction with a multiplexer, can successively read out the information from several charge-coupled devices.

Lines of charge-coupled devices can also be used in the "trigger-recording" regime in which the increase in the cell address by unity occurs only on the arrival of a pulse at the input of the charge and time converter.[93]

Recently, selection–storage schemes based on charge-coupled devices have made their appearance. The use of such schemes in the form of an analog memory makes it possible to increase the speed of the charge and time conversion (rate of recording in a cell $\lesssim$10 nsec) and eliminate distortion of the charge due to its multiple transfer in the lines of the charge-coupled devices. Charge and time conversion using a selection–storage scheme based on charge-coupled devices is described, for example, in Ref. 93.

Electronics channel with fast ADC. The most elegant variant of the electronics is based on the use of fast ADCs. Recently there have appeared six- and eight-bit superfast monolithic ADCs with conversion time down to 10 nsec.[142] Use of them makes it possible to convert pulses arriving from the chamber directly in the real time scale. Such a read-out system was used, for example, in the development of the central detector of the UA-1 facility at CERN.[143]

A charge–time converter based on such ADCs can be obtained relatively easily (Fig. 28). It includes two fast amplifiers, two integrators, two fast ADCs, a control circuit, a time-measurement circuit, and a fast buffer memory.

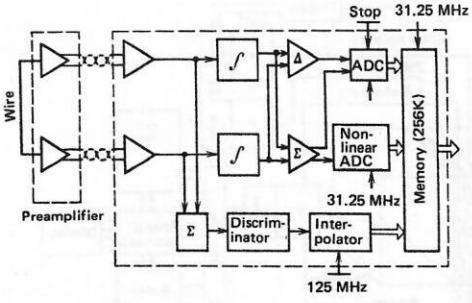

FIG. 28. Scheme of charge and time conversion with fast ADCs.[143] $\int$ is an integrator, Σ is a summator, and Δ is a device that determines the difference between pulse heights.

The charge–time converter in the central detector of the UA-1 facility makes it possible to measure the charge and also the coordinate along the sense wire by the current-division method. In these charge–time converters six-bit ADCs with conversion time 33 nsec are used. By means of a regulated reference voltage it proved possible to extend the dynamic range to nine bits.[144] The time is measured to an accuracy of 4 nsec by means of a time interpolator.[134]

Finally, let us attempt to compare the methods of analyzing information from multilayer drift chambers. The use of an analog memory based on capacitors is laborious, does not ensure reliable operation, and is not promising. Converters from the analog memory based on charge-coupled devices are more progressive, but charge-coupled devices are sensitive devices, and it is necessary to ensure conditions for reliable operation when they are used. It is necessary to increase the recording frequency f_1 to 20–50 MHz, and then information about the pulse arrival time will also be contained in the charge-coupled devices.[141]

The use of fast ADCs is the most promising. The electronics channel is relatively simple, which ensures reliable operation of the large system. At the moment, the main obstacle to the use of fast ADCs is their high cost. As regards the accuracy of charge measurement, they are inferior to charge-coupled devices.

The flux of information from multilayer drift chambers. A multilayer drift chamber generates a large flux of information, since the coordinate and charge are measured at 250–300 points on each track. The charge is usually measured with an accuracy of six to eight bits; to measure the coordinate, one needs about eight bits, and therefore information about one point of the track on one wire can be put into one 16-bit word. If the energy of the primary particle is about 50 GeV, the multiplicity of the charged particles is $N_{ch} \approx 5$; at an energy of order 1 TeV, it is $N_{ch} \approx 10$. Thus, if several noise pulses are present in each channel, a chamber with 250 layers generates about 5K words per event.

If a minicomputer (for example, of the type EC-1010) with operative memory of 32K words is used, the information must be stored on a magnetic disk. This slow operation requires 100–120 msec to store one

event. Such a system makes it possible to record not more than eight or ten events per second. The use of a computer with a larger memory, for example, 128K words (SM-4-20 or PDP 11/70) makes it possible to keep information in the operative memory without using disk and to record 25–30 events per second.

A sharp increase in the rate of accumulation of statistics can be achieved by using a fast buffer memory. Thus, information from the chamber ISIS is stored in the buffer memory with frequency 110 nsec/word.[145] At this rate, it is possible to record one event in about 5 msec.

The transfer and fast analysis of the large flux of information from multilayer drift chambers is not a simple problem. For example, the flux of information from the facility UA-1 is about 1 Mbyte/sec. Only the use of modern electronics, including specialized processes and a fast buffer memory, makes it possible to accumulate the necessary statistics at a sufficient rate.

3. IDENTIFICATION OF HIGH-ENERGY PARTICLES BY MEANS OF THE PRIMARY IONIZATION

The relativistic rise of the primary ionization in gases (see Fig. 3a), like the rise of the ionization energy loss, can be used to identify particles. In some experiments, the first method is preferable on account of its simplicity and greater accuracy. Thus, the fluctuations of the primary ionization follow a Poisson distribution, which is narrower and more symmetric than the distribution of the energy loss (see above). The primary ionization can be measured in track detectors simultaneously with measurement of the momentum on the basis of the track curvature in the magnetic field. The expected value of the relativistic rise of the primary ionization in gases at $P=1$ atm is 1.4–1.6 (see Table I).

Several ways are known for determining the primary ionization produced by charged particles in gas:

1) measurement of the density of primary pairs of ions on the track in a Wilson chamber or diffusion and streamer[8)] chambers;

2) by counting the clusters (bunches of electrons on the track of the particle) as they drift along the direction of the track to the anode wires of the drift chamber;

3) by using the efficiency of a gas-discharge detector (Geiger counter, discharge tube, spark or proportional chamber);

4) by the discharge formation time in a spark chamber.

These methods all differ in their accuracy, the extent to which they have been developed, and the amount they are used. Thus, streamer chambers have already been used to identify relativistic particles. The cluster-counting method and low-pressure spark chambers have also been tested in physics experiments. However, only the first steps have been made in the development of the method of measuring the primary ionization by determining the formation time of a spark discharge.

Measurement of primary ionization in a streamer chamber

Conditions of measurement of primary ionization in a streamer chamber. The streamer chamber[146,147] developed in 1963 almost completely displaced from nuclear-physics experiments classical track detectors such as the Wilson chamber and the diffusion chamber, which can measure primary ionization.[148,149] The properties and features of streamer chambers, their use in experimental physics, and also ways of generating the high-voltage nanosecond pulses needed for their operation are described in detail in Refs. 2, 9, and 150–156. Here, we shall restrict ourselves to questions relating to the use of streamer chambers as ionization identifiers of relativistic particles.

The tracks of particles in a streamer chamber are chains of short ($\lesssim 1$ cm) luminous streamers or avalanches of diameter $d_s \sim 1$ mm, which are elongated along the field and develop on ionization electrons. It was already noted in the early studies[157,158] that the ionizing capacity of particles could be measured by the mean number g_s of streamers per unit track length (the density of streamers), and also by their brightness b_s and length l_s. However, it was found that the last two parameters are unsuitable for exact measurements of the ionization because of their strong dependence on the characteristics of the high-voltage pulse and the angle formed by the track and the direction of the electric field,[159] and also because of their inherent large fluctuations.[160]

To obtain bright streamers suitable for direct photographing, one requires a streamer length $\gtrsim 1$ cm.[157,158,160] However, the density of streamers in the tracks of relativistic particles is only 2–3 cm^{-1}, remaining several times less than the specific primary ionization[34] and varying weakly when the latter increases.[159,161] Only for $l_s \ll 1$ cm, when the track consists of very short weakly luminous streamers (or avalanches that have not yet developed into streamers), is their number close to the number of primary electrons.[34,158,160,162] Such a track is not at all bright, and special methods must be used to detect it.

The conditions under which it is possible to measure the primary ionization in a streamer chamber were already investigated more than 10 years ago, primarily in studies of a group at the Moscow Engineering Physics Institute,[34,160,162-166] and they are follows:

1) the streamer chamber must operate in a regime that precludes electric interaction between the streamers, which tends to reduce their number;

2) the mean length l_d of diffusion during the time τ_d of delay of the high-voltage pulse relative to the time at which the particle passes must be much less than the measured radius r_s of the streamer (r_s depends on the

[8)] The name *streamer* chamber is below also extended to *avalanche* chambers, in which the discharge in the gas is terminated at the avalanche and not the streamer stage.

detection method and the optical characteristics of the detecting system);

3) the characteristic times of the processes of the electron and atom collisions in the gas that influence the number of electrons in the track must be much longer than τ_d;

4) the sensitivity of the detecting system must be sufficient to detect the faintest streamers;

5) the analysis of the photographs of the tracks must take into account geometrical overlapping of the streamer images.

If these conditions are satisfied, the results of the measurements of the ionization do not depend on the fluctuations in the operating regime of the streamer chamber (in the shape, amplitude, and delay time of the high-voltage pulse, or in the length and brightness of the streamers).[34] Let us consider these conditions in more detail.

Influence of processes in the gas of the streamer chamber. Interaction of streamers. The electric interaction between streamers can lead to their coalescence, and also to a slowing down in the growth and even to a suppression of delayed streamers, which develop in the electric field distorted by the space charge of the neighboring streamers. Such effects are associated with appreciable fluctuations in the development of the streamers and are enhanced with increasing l_s because of the rapid rate of growth of a streamer with its length.[160,163] For this reason, the efficiency of detection of primary electrons when $l_s \gtrsim 1$ cm is always less than 100% (Fig. 29). One can eliminate interaction between streamers by reducing their length to $l_s \ll 1$ cm by shortening the high-voltage pulse to $\tau_h \lesssim 10$ nsec,[158] by reducing the gas pressure,[34,166] or by using gases with low Z.[34,167]

Diffusion of secondary electrons. If during the time τ_d the diffusion of the secondary electrons is slight, i.e., $l_d \ll r_s$, either they can be detected as individual streamers or they have the form of a characteristic branching in the track (in the case of a large energy transfer in the collision) and can be rejected during analysis (Figs. 30a and 30b). In this case, the primary ionization can be measured. In the case of large τ_d,

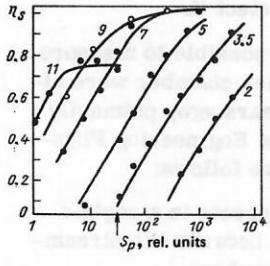

FIG. 29. Dependence of the efficiency η_s of streamer detection on the sensitivity S_p of the photographic system ($P = 0.8$ atm, Ne). The numbers next to the curves correspond to the mean length l_s (mm) of the streamers; the arrow indicates the sensitivity threshold of the detection system in the case of direct photography with aperture $a_p = 1:1.5$.[160]

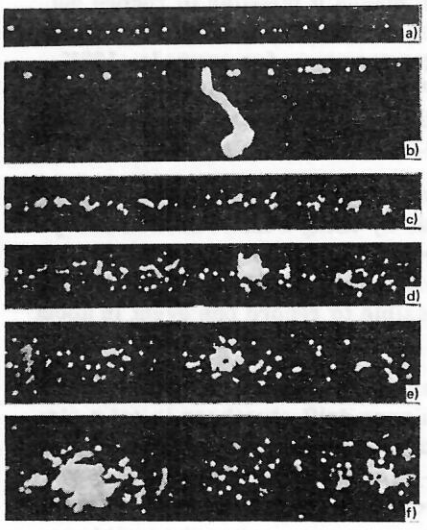

FIG. 30. Tracks of relativistic particles in a streamer chamber: a) and b) He, $P = 0.6$ atm; c)–f) Ne, $P = 0.8$ atm. The delay time of the high-voltage pulse: a) and b) 0.2 μsec; c) 1 μsec; d) 2.5 μsec; e) 5 μsec; f) 10 μsec.[34]

when $l_d \gtrsim r_s$, a streamer grows on every secondary electron (see Figs. 30c–30f), which makes it possible to measure the total ionization (see Fig. 5).

The influence of electron diffusion in pure He, Ne, and Ar is shown in Fig. 31. For $\tau_d \gtrsim 0.2$ μsec it is only in He that g_s does not depend on τ_d and corresponds to the primary ionization. These calculations are made for purely thermal diffusion of the electrons. In reality, the initial energy of the secondary electrons is close to the first excitation potential of the atoms, and they are only gradually thermalized in elastic collisions. Therefore

$$l_d = (l_T^2 + l_D^2)^{1/2}, \tag{41}$$

where l_T and l_D correspond to the diffusion during the thermalization time and after it. As a rule, thermalization increases the diffusion compared with purely thermal diffusion (Fig. 32).[168]

The electron diffusion can be reduced by introducing into the gas special additives, since the diffusion coefficient for a mixture of gases is

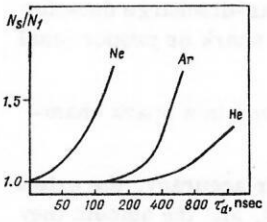

FIG. 31. Dependence of the ratio of the expected number N_s of streamers to the number of primary collisions N_1 on the delay time τ_d of the high-voltage pulse. The calculations were made for a streamer radius $r_s = 0.4$ mm and the following values of the coefficients of thermal diffusion of the electrons: $D_{He} = 312 \pm 14$ cm^2/sec (Ref. 34); $D_{Ne} = 3000 \pm 174$ cm^2/sec (Ref. 164); $D_{Ar} = 270$ cm^2/sec (Ref. 168).

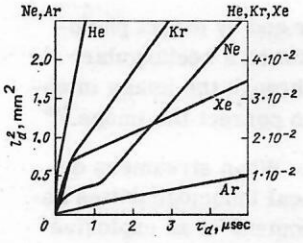

FIG. 32. Dependence of the mean-square diffusion length l_d^2 of electrons in noble gases under normal conditions on the delay time τ_d of the high-voltage pulse. A constant slope of a curve corresponds to thermal diffusion.[168] (Calculations were made using data on momentum-transfer cross sections.[169])

$$D = [\sum_i (a_i/D_i)]^{-1}. \quad (42)$$

Here, a_i is the relative concentration, and D_i is the diffusion coefficient of component i. For this reason, in particular, mixtures of He and Ne are more suitable for ionization measurements in a streamer chamber than pure Ne.[34,166]

The electron diffusion is very effectively reduced by many molecular impurities, in which the presence of low-lying excitation levels leads to rapid thermalization, and the thermal diffusion is strongly reduced by virtue of the large collision cross section with thermal electrons. Thus, the thermalization time can be appreciable shortened by small (about 1 torr) additions of N_2, N_2O, and H_2O, which hardly influence the thermal diffusion.[164] In turn, the latter is reduced by tens of times in the presence of CO_2 and C_6H_6 or saturated C_2H_5OH and H_2O vapor[34,164,170] (see also Table X). Electron diffusion is also appreciably reduced in the presence of a magnetic field,[176] which is particularly important when a low-pressure streamer chamber is used.[165,177] Reduction of the electron diffusion simultaneously improves the accuracy of the measurements of the momenta of the particles and the primary ionization.

Inelastic electron and atom collisions in the gas. Collisions involving electrons and excited atoms in the gas of the streamer chamber during the time τ_d between the passage of the particle and the time at which it is detected can change the initial number of electrons on the track of the particle. The relevant collision processes are as follows:

TABLE X. Cross sections of momentum transfer σ_m and attachment σ_e for thermal electrons in molecular gases ($\mathscr{E}=0$).[29,171-175]

Gas	σ_m, cm^2	σ_e, cm^2
N_2	$4\cdot10^{-16}$	$\approx 10^{-23}$
O_2	$3\cdot10^{-16}$	$\approx 10^{-22}$
I_2	—	$3\cdot10^{-15}$
H_2O	$7.5\cdot10^{-14}$	$(7.5\pm0.6)\cdot10^{-21}$
N_2O	$2.2\cdot10^{-15}$	$<10^{-17}$
CH_4	$6\cdot10^{-16}$	—
CO_2	$1.08\cdot10^{-14}$	$<10^{-20}$
C_3H_8	$\approx 10^{-15}$	—
C_6H_6	$1.2\cdot10^{-14}$	$\approx 10^{-16}$
CCl_4	—	$2.6\cdot10^{-14}$
SF_6	—	$(1.7\pm0.2)\cdot10^{-14}$
i-C_4H_{10}	$1.4\cdot10^{-15}$	—
CF_2Cl_2	—	$<10^{-18}$

1. Attachment of electrons to impurities. Because of attachment, the number N_e of secondary electrons decreases exponentially with time:

$$N_e(\tau) = N_e(0)\exp(-\tau/\tau_e). \quad (43)$$

Here,

$$\tau_e(c) \approx 3\cdot10^{-20}/(\bar{v}_e \sum_i P_i\sigma_{e,i}) \quad (44)$$

is the attachment time constant, $\bar{v}_e \approx 1.19\times10^7$ cm/sec is the mean velocity of the thermal electrons, and P_i and $\sigma_{e,i}$ are the pressure (atm) and the attachment cross section of component i of the mixture (see Table X). Attachment can be ignored if $\tau_e \gg \tau_d \approx 1$ μsec, i.e., when

$$\sum_i P_i\sigma_{e,i} \ll 3\cdot10^{-18}\ \text{cm}^2\cdot\text{atm}. \quad (45)$$

2. Ionization of atoms and impurity molecules (Y) in collisions with the excitation of metastable atoms (X^*) of the main gas (Penning effect):

$$X^* + Y \rightarrow X + Y^+ + e^-. \quad (46)$$

Because of this, the measured primary ionization in a mixture of gases is larger than the sum of the primary ionizations of its components. The characteristic time of the reaction (47) is determined by a relation analogous to (43) (the mean relative velocity of the atoms X^* and Y is $\bar{v}_a \approx 10^5$ cm/sec). The contribution of the Penning reaction, which has cross section $\sigma_P = 10^{-16}$–10^{-15} cm^2,[172-174] is small if

$$\sum_i P_i\sigma_{P_i} \ll 10^{-16}\ \text{cm}^2\cdot\text{atm}. \quad (47)$$

The error in the measurement of the primary ionization associated with the Penning reaction can exceed 10% in a gas with impurities.[162]

3. The formation of molecular ions of the noble gases (X_2^+, XY^+) in collisions of resonantly excited and neutral atoms:

$$X^* + X \rightarrow X_2^+ + e^-; \quad (48)$$
$$X^* + Y \rightarrow XY^+ + e^-. \quad (49)$$

Contributions to these reactions, which take place with a cross section of about 10^{-15} cm^2,[174] are made by levels with excitation energy above the potential for the formation of a molecular ion. Therefore, the reaction (48) is possible only in He. At pressures $P_i \gtrsim 10^{-1}$ atm, these processes take place effectively instantaneously, so that the additional ionization caused by them (which is a few percent) cannot be separated from the primary ionization.

The electron and atom collisions in the gas distort the measured primary ionization but do not affect its relativistic rise.[165,178] At the same time, something of value can be extracted from them. The attachment effect is used to shorten the memory time,[175,179] and the reactions (46), (48), and (49) can be used to record track information (in the regime of two-pulse feeding of the streamer chamber) for a time up to 10^{-2} sec without loss of spatial accuracy.[180,181]

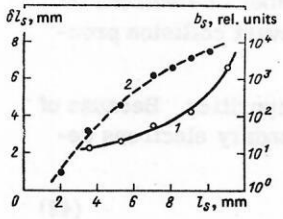

Fig. 33. Dependence of the spread δl_s of the length (1) and brightness b_s (2) of a streamer on the mean streamer length l_s.[160]

Detection of particle tracks. At the present time, two methods are used in streamer-chamber work:

1) detection of the actual emission of the streamers or avalanches;

2) photography in laser light of the transparent inhomogeneities of the gas due to the streamers.

Detection of the streamer emission. The brightness of a streamer depends very strongly on its length,[160] so that even small fluctuations in the length of streamers lead to strong fluctuations in their brightness (Fig. 33).

This can easily cause the loss of an appreciable fraction of the streamers, since it is comparatively easy to photograph the brightest of them, whereas the detection of all 100% of the streamers is much more complicated.

To solve this problem, the detecting system must meet the following requirements:

1) it must detect streamers with $l_s < 1$ cm, for which there is no coalescence of the streamers, the fluctuations of the length are small, and the brightness is more uniform;

2) the dynamic range of its sensitivity must be greater than the span of the brightness fluctuations of the streamers.

As is shown in Fig. 29, weakly luminous streamers and avalanches are beyond the detection threshold for direct photography. The reason for this is that an avalanche emits about 10^8 photons/mm^2 (a streamer of order 10^{10} photons/mm^2) and if the photographing is done with reduction coefficient $K_p \approx 50$ and aperture $a_p \approx 1/8$, the light flux is reduced by 10^3 times, whereas the sensitivity threshold of standard photographic film is about 10^8 photons per 1 mm^2. Therefore, to detect tracks in a streamer chamber it is necessary to use image intensifiers (see Refs. 34, 158, 162–166, and 182–190 and Table XI). Since photography of the screen of an image intensifier also involves large light losses, the image-intensifier enhancement must reach $K = 10^5$–10^6 (for $K_p \approx 50, a_p = 1/8$) (Ref. 156) and $K = 10^3$–10^4 (for $K_p \approx 5, a_p = 1/1.5$).[34,158] These losses can be avoided by using fiber optics or by directly detecting the electron image (electron diffraction).[156]

The use of an image intensifier introduces appreciable optical distortions and the space resolution is less good. Therefore, in simultaneous measurements of the ionization and momentum the tracks are detected separately (with an image intensifier and by direct photography, respectively[183]). Sometimes a rectangular luminous grid is photographed through the image intensifier, this making it possible to correct the image.[195]

Laser detection of streamers. When streamers develop in a gas, transparent optical inhomogeneities associated with gas-dynamic phenomena of an explosive nature are formed. Because of the reduced refraction of the gas, such inhomogeneities perturb a passing light wave, and they can be photographed if illuminated by a laser.[196] It is easier to detect the streamers, the larger the coefficient of refraction, the higher the pressure, and the lower the temperature of the gas.[197] Thus, the quality of the images of the tracks in H_2 and CH_4 and mixtures of them is much better than in He, although the streamers are much brighter in the latter.

For the detection of the transparent inhomogeneities produced by streamers in the gas, two methods have been proposed: holograms and laser shadowgrams.[196,198] The latter are obtained by taking a cine film in laser light of the shadows of the streamers on a diffusely reflecting or a directionally scattering screen, or directly on photographic film. To obtain sterographic photographs, the light rays must differ in either color or polarization and the camera must have appropriate light filters. The flash of the pulsed laser is synchronized with the pulse from the charged particle, and for a laser with long (>1 μsec) delay of its flash (for example, a ruby laser) two-pulse feeding of the streamer chamber is used.[198]

The use of this method is extremely promising, since it completely eliminates the problem of photographing weakly luminous streamers. Laser illumination considerably increases the streamer detection efficiency (Fig. 34), the spatial characteristics of the track, and the accuracy of the measurement of the primary ionization (Table XII). It allows one to photograph in a hydrogen streamer chamber tracks so faint that they cannot be seen even after prolonged adaptation to the dark by the eye.[193]

Measurement of ionization using the tracks of particles in a streamer chamber. Influence of overlapping of the images of the streamers. The overlapping of the images of streamers, which is a consequence of their finite size and random distribution along the track, and also the imperfection of the optical detection system, reduces the accuracy of ionization measurements.

The influence of the overlapping of the images of structural elements of the track has been considered in connection with bubble chambers,[199] nuclear emulsions,[200] Wilson chambers,[149] and streamer chambers.[201,202] Methods have been proposed for determining the ionization on the basis of directly measured parameters of the track—the integral and differential distributions of the lengths of the intervals (gaps) between the elements (blobs) of the track, the mean length of a gap or a blob, the density of the gaps or the blobs, the number of empty intervals in the track (Refs. 149, 199, 200, and 202), and also a method of correct measurement of the density of streamers.[201] The majority of

TABLE XI. Use of streamer chambers for measurements of primary ionization and identification of high-energy particles (1980 data).

Group	Measurements of streamer chamber, cm³	Filling	P, atm	Amplitude and duration of pulse	Method of detection of streamers	Particles and their energy (momentum)	Experiment
Lehigh University, USA[167]	20.3×12.7×2.5	He	1 0.2	25 kV, 40 nsec	Direct photography	p, 0.6—2 GeV/c	Study of streamer-chamber properties
Moscow Engineering Physics Institute[34,162,166]	30×18×3.5	He 50% He+50% Ne 49% He++49% Ne++2% H_2O	0.6 0.84 0.13	— — —	Photography with image intensifier $K=10^3$	e^-, 2—570 MeV	Measurement of primary ionization and its relativistic rise
CERN, Geneva[158,162]	11×10×10	30% He+70% Ne	1	300 kV, 5 nsec	Photography with image intensifier	Secondary beam of hadrons, 27 GeV/c	Searches for fractionally charged quarks
DESY, Hamburg[179]	100×60×(2×16)	25% He++75% Ne++10^{-6}% SF_6 He+10^{-6}% SF_6	1	350 kV, 10 nsec	Direct photography, $K_p=1/38$ $a_p=1/2$	Tagged photons, 1.8-7 GeV	Photoproduction of hadrons on hydrogen
Physics Institute, Aachen[184,185]	100×30×16	95% He+5% Ne 50% He+50% Ne	0.9 1.0	400 kV, 6 nsec	Photography with image intensifier $K=10^5$	Cosmic rays	Searches for quarks in extensive air showers
CERN, Geneva[187]	55×35×(2×10)	H_2+0.5% CH_4++$5\cdot10^{-5}$% SF_6	1.0	650 kV, 3 nsec	Photography with image intensifier $K=2\cdot10^4$	Cosmic-ray particles; e^-, 2 MeV	Investigation of the properties of a hydrogen streamer chamber
Leningrad Institute of Nuclear Physics[191,192]	15×15×5	70% He+30% CH_4	1.0	200 kV, 20—40 nsec	Laser shadowgraphy	p^+, 1 GeV e^-, 2 MeV	The Skalar facility. Investigation of proton-nucleus interactions
Leningrad Institute of Nuclear Physics and JINP[193]	20×20×6	H_2	0.4—1.0	180 kV	Laser shadowgraphy	e^-, 2 MeV	Leningrad Institute of Nuclear Physics and JINR[194]
CERN, Geneva[186,177,194]	270×125×(2×25)	30% He++70% Ne++0.3% i-C_4H_{10}++10^{-5}% SF_6	1.0	400 kV, 15 nsec	Photography with image intensifier	π^-, K^-, $\bar{p}$; 16 GeV/c	Experiment NA-5. Investigation of inelastic $p\bar{p}$ interactions
CERN, Geneva[188]	235×125×(2×30)	80% He+20% Ne	1.0	600 kV, 10 nsec	Photography with image intensifier	Charged products of neutrino interactions	Experiment WA-44. Searches for quarks in high-energy neutrino interactions
JINR, Dubna[183,189]	500×120×(2×40)	30% He++70% Ne++10^{-4}% SF_6	1.0	800 kV, 10 nsec	Photography with image intensifier $K=10^5$	π^-, K^-, $\bar{p}$; 25—40 GeV/c	The experiment Risk. Interaction of π^-, K^-, and $\bar{p}$ with nucleons and nuclei
CERN, Geneva[190]	600×120×(2×40)	30% He++70% Ne++10^{-4}% SF_6	1.0	800 kV, 10 nsec	Photography with image intensifier	$p+\bar{p}$, (270×2) GeV/c	Experiment UA-5. $p\bar{p}$ interactions at 540 GeV (c.m.s.)

these parameters depend not only on the track density but also on the minimal length l_m of a gap at which the images of neighboring streamers can be distinguished. Therefore, any two of the listed parameters are mutually independent, and simultaneous measurement of them gives a more accurate estimate of the ionization.[202]

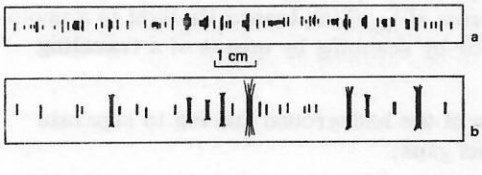

FIG. 34. Images of a section of the track of a 1-GeV proton in a streamer chamber obtained simultaneously by the laser-shadowgraph method (a) and by direct photography (b) at the angles 40° and 50°, respectively, to the direction of the electric field. Filling 70% He+30% CH_4, $P=1$ atm.[191]

TABLE XII. Characteristics of the images of the tracks of protons (1 GeV) and electrons (2 GeV) in a streamer chamber filled with a 70% He+30% CH_4 mixture.[191,192]

Method of detection	d_s, mm	l_s, mm	l_d, mm	g_s, cm^{-1}	
				p	e^-
Direct photography	1.53±0.04	6.33±0.25	0.240±0.022	2.50±0.05	—
Laser detection	0.38±0.01	2.40±0.09	0.195±0.011	8.20±0.06	7.80±0.10
Results of calculation	—	—	0.186	—	7.4

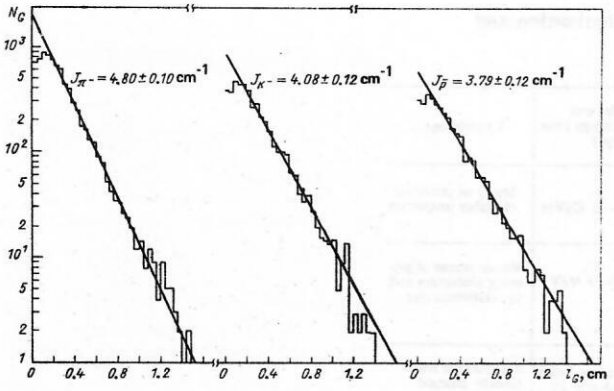

FIG. 35. Integral distributions of the length l_G of the gaps between streamers on the tracks of particles in a streamer chamber filled with 30% He + 70% Ne + 10^{-5} SF_6 mixture ($P = 1$ atm). The slope of the approximating curves determines the measured ionization J. A departure of $N_G(l_G)$ from a linear dependence is observed when $l_G < l_m = 0.25$ cm.[178]

In streamer-chamber experiments, the following methods are used to analyze the tracks:

1. The method of Ref. 162, in which one counts the number of "empty" intervals of given length $l_0 > l_m$ along the track, i.e., intervals not containing centers of streamers. The probability W_0 of finding such an interval is

$$W_0 = \exp[-(dN_1/dl)\, l_0]. \quad (50)$$

This method is convenient for rapid analysis but has low accuracy.[199]

2. From the slope of the integral distribution of the gap lengths (GD) (Refs. 149, 178, 184, 185, and 202). In the case of a random distribution of the streamers along the track, the number of gaps with length $l_G > l_0$ decreases exponentially (Fig. 35):

$$N_G(l_G > l_0) = N_G(l_G > 0) \exp[-(dN_1/dl)\, l_0]. \quad (51)$$

The deviation from this dependence when $l_0 < l_m$ is due to the finite optical resolution, and also the electric interaction of closely spaced streamers. We note that diffusion of electrons along the track (when the condition $l_d \ll r_s$ is satisfied) does not affect the results of the measurements, since it preserves the random nature of the streamer distribution. (Transverse diffusion has no influence at all on the length of the gaps.)

3. From the density of streamers (SD) on the track (Refs. 178, 184, 185, 201, and 202). In this method, one counts the number N_s of streamers over the length L of the track, each streamer being at a distance $l_G > l_m$ from the preceding counted streamer. The count is made in one direction, and $l_m > d_s = 2r_s$ is chosen experimentally to ensure that the results of the measurement do not depend on l_m. If $L \gg l_m$, then[201]

$$(dN_1/dl) = N_s/(L - l_m N_s). \quad (52)$$

4. From the mean lengths of the gaps (LG) or the blobs (LB), the density of the gaps (DG) or the blobs (DB), and the "emptiness" of the track (ET).[194, 200, 202]

TABLE XIII. Accuracy of measurement of the primary ionization on the tracks of relativistic particles in a streamer chamber filled with 50% He + 50% Ne mixture ($P = 0.9$ atm, $K_p = 1/30$).[202]

Method of measurement	L, m	l_m, mm	dN_1/dl, cm^{-1}	Error of measurement of the ionization of an individual track, %	
				total	statistical
SD	0.22	1.5	6.26±1.12	17.8	—
LG	0.22	3.0	6.48±1.41	21.8	22.0
LB	0.22	3.6	5.75±1.26	21.9	13.8
DG	0.22	3.6	6.39±1.06	16.6	15.0
ET	0.22	3.6	6.49±0.97	14.9	13.4
GD + LB	0.22	3.6	6.08±1.12	18.4	12.0
GD + ET	0.22	3.6	6.48±1.02	15.9	—
DG + ET	0.22	3.6	6.45±0.96	14.9	—
GD	11	3.0	6.5±0.2	3.1	—
LG	11	3.0	6.5±0.2	3.1	—

An idea of the accuracy of these methods is given by Table XIII.

The overlapping of the streamer images prevents an improvement in the accuracy of measurements of the ionization with increasing g_s (resulting from an increase in the pressure or the use of heavy gases). The optimal density of streamers when $l_s = 1$–2 mm is 6–8 cm^{-1}.[165] Such a density can be readily obtained in He + Ne mixtures, which in addition give bright streamers and the maximal relativistic rise of the primary ionization.[17] Then the expected rms error of the measurement of the primary ionization over 1 m of track is 4–4.5% and decreases in proportion to $L^{-1/2}$. Under real conditions, such accuracy cannot be achieved (Table XIII). This is due to the loss of an appreciable fraction of the statistics due to the finite value of l_m, and also to systematic errors.

The overlapping of the streamer images becomes stronger with increasing angle θ of the particle trajectory relative to the plane of the electrodes of the streamer chamber. However, measurements of the primary ionization for $g_s = 6$–8 cm^{-1} are possible up to $|\theta| \leq 30°$.[165]

Automation of ionization measurements. For automation of ionization measurements in the case of the analysis of photographs in streamer chambers, the same principles and instruments as for bubble chambers are used. The procedure of analysis consists of the following stages:

1) the search for events (by examination[194, 202] or automatic scanning[178, 195]);

2) determination of the coordinates and photometry of the track using automatic or semiautomatic measuring devices, the photometry being done by moving the track across a narrow slit, which transmits light to a photometer,[194, 202] or by scanning by means of a traveling beam[178, 195];

3) filtration of the background and fog to separate streamers and gaps;

4) calculation of the ionization parameters of the track and the primary ionization.

The automatic analysis of one frame occupies 15–20 sec. The efficiency of the track search does not depend

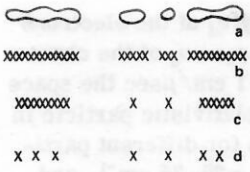

FIG. 36. Stages of automatic analysis of a track section in a streamer chamber: a) section of the track; b) results of digitizing; c) correction to take into account spreading of the streamer images; d) streamers used to determine the primary ionization.[178]

on the number n_M of events in the frame (for $n_M < 10$), the density (for $g_s \geq 0.25$ cm^{-1}), or the position of the track in the streamer chamber.[195] The inability of automatic devices to distinguish faint streamers can lead to a systematic lowering of the measured ionization. However, since the ionization measurements are normalized by beam particles, this does not influence the reliability of identification.[194,195] The sequence of steps in the automatic analysis of a track (the measurement of g_s) using scanning with a traveling beam is shown in Fig. 36.[178]

There is also an essentially new way to automate the ionization measurements, namely, filmless detection of tracks by means of systems operating on line to a computer. For this, one can use high-sensitivity TV tubes[203,204] or solid-state light-sensitive matrices of charge-coupled devices and charge-injection devices.[205] Both methods are highly light-sensitive and have good space resolution, a wide dynamic range, and short dead time. In addition, the matrices are insensitive to external magnetic fields. Devices based on TV tubes[206-210] and charge-coupled devices[211,212] have already been tested for coordinate measurements in streamer chambers. The recovered images of the tracks repeat their structure,[206,212] which indicates the possibility of automation of the ionization measurement. It is evidently expedient to combine image detectors of the TV-tube or charge-coupled-device (charge-injection-device) type with an image-intensifier exit cascade.[210] They are also conveniently used in the case of laser detection of tracks in a streamer chamber.

Relativistic rise of the primary ionization and identification of particles in a streamer chamber. The relativistic rise and the plateau of the primary ionization were investigated experimentally for the first time in a helium Wilson chamber[149] and in a streamer chamber filled with helium[162] and He+Ne mixtures.[165,178] The obtained data (Fig. 37) agree well with the theory of primary ionization,[17] which can serve as a basis for estimating the accuracy of measurements needed for reliable identification of relativistic hadrons (see Refs. 156, 165, 185, 202, and 213–215).

The problems of identifying high-energy particles using the relativistic rise of the primary ionization and the probable energy loss (see Sec. 2) have much in common, since the corresponding dependences are similar in their behavior and in the scale of the relativistic rise (see Figs. 3a and 3d). The relative difference of the

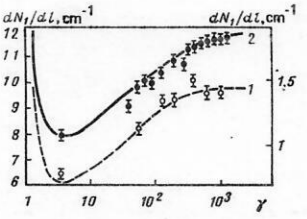

FIG. 37. Relativistic growth of the specific primary ionization measured in a streamer chamber: a) 49% He+49% Ne +2% H_2O, $P = 0.13$ atm (right-hand scale); b) 50% He+50% Ne, $P = 0.84$ atm (left-hand scale).[166] The smooth curves are the predictions of the theory of primary ionization.[17]

primary ionization in the region of logarithmic growth, for example, for $p = 10$ GeV/c, is approximately 25% for π/p, 15% for π/K, and 8% for K/p. The reliability of the particle identification depends weakly on the rms error $\langle \delta p/p \rangle$ in the measurement of the momentum in the streamer chamber and is basically determined by the accuracy $\langle \delta J/J \rangle$ of the ionization measurements[213]:

$$\langle \delta m/m \rangle \approx [(\langle \delta p/p \rangle)^2 + (7\ \langle \delta J/J \rangle)^2]^{1/2}. \quad (53)$$

Therefore, to identify hadrons with 90% confidence the accuracy of the ionization measurements must be about 3%. Theoretically, this can be achieved for $g_s = 6$–8 cm^{-1} if the track length is $L = 1$ m. Under real conditions, because of the overlapping of the streamer images and systematic errors, such accuracy is achieved only when $L \gtrsim 4$ m (see Refs. 165, 185, 202, 213, and 215).

The possibility of identifying the relativistic hadrons π, K, and p in a streamer chamber is demonstrated in Fig. 38. (The maxima of the curves in the left-hand part of the figure go to infinity, since they correspond to the intersection of the relativistic and nonrelativistic branches of the curves shown in Fig. 3a, and also in Fig. 37, and refer to different particles.)

It can be seen that a lowering of the gas pressure does not permit a significant advance into the region $p > 200$ GeV/c because of the deterioration in the statistical accuracy of the measurements of the primary ionization.

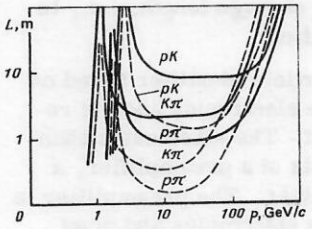

FIG. 38. Length of streamer chamber needed to identify hadrons with 90% confidence. The continuous curves correspond to 49% He+49% Ne+2% H_2O mixture and $P = 0.13$ atm; the broken curves, to 50% He+50% Ne mixture and $P = 0.84$ atm; the left-hand parts of the curves correspond to nonrelativistic hadrons.[166]

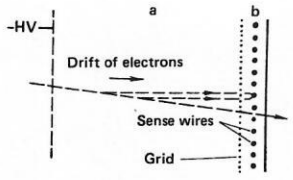

FIG. 39. Arrangement of drift chamber for cluster counting: the drift gap is A, the gas-amplification gap is B, and HV denotes a high voltage.

Cluster-counting method in a chamber with slow drift of the electrons

Walenta recently proposed a new method for measuring primary ionization in a drift chamber by cluster counting. (By a cluster one means a collection of secondary electrons on the track of the particle formed by one primary particle.) Walenta constructed and tested a small chamber for counting clusters with a drift gap of length 10 mm and gas-amplification gap of 3 mm.[114] In this chamber it was possible to count clusters down to individual electrons. Figure 39 shows the scheme of a drift chamber of this type. It consists of two main parts: the drift volume and the gas-amplification gap (proportional chamber). The particles pass through the chamber at right angles to the plane of the sense wires. In the drift gap the electrons drift slowly under the influence of an electric field along the particle track. They readily pass through the grid into a region in which there is a stronger field, and the gas amplification occurs near the sense wires.

In ordinary drift or proportional chambers, the collection of the electrons from the particle track occurs rapidly, the entire charge after the gas amplification is integrated, and as a result one pulse is produced. In a chamber with cluster counting, a weaker electric field is produced, so that the clusters drift slowly to the sense wires. After gas amplification at a sense wire a series of pulses is formed, each of them corresponding to one cluster. Thus, if the electron drift velocity is $v_d = 1$ cm/μsec, the mean time interval between the pulses is 30–40 nsec. After multiplication, the pulses can be counted by a fast counter. Thus, this method makes it possible to measure the number of clusters in a section of track of given length, i.e., to determine the primary ionization.

The main advantage of a particle identifier based on cluster counting is the simple electronics and the reduced length of the instrument. The electronics channel for one sense wire consists of a preamplifier, a discriminator, and a fast counter. The preamplifier is the most important link in the electronics and must meet high requirements with regard to the input sensitivity, the linearity, and dead time.

Lapique and Piuz[76] analyzed in detail the conditions of cluster counting in a chamber with slow drift of the electrons. The time resolution τ of the electronics is determined by the dead time of the preamplifier and the counter, and for fixed drift velocity v_d of the electrons it determines the space resolution $\rho_x = \tau v_d$ of the chamber. Thus, for $\tau = 10$ nsec and $v_d = 1$ cm/μsec the space resolution is $\rho_x = 0.1$ mm. For a relativistic particle in argon the mean number of clusters for different particle momenta lies in the interval $N_1 = 25$–35 cm^{-1}, and the corresponding mean distance between clusters is $d_c \approx 0.28$–0.4 mm. The statistical fluctuations of the distance between the clusters for $\rho_x = 0.1$ mm leads to their overlapping, which reduces the counting efficiency to $\eta = N_c/N_1 \approx 0.75$, where N_c is the number of counts of the counter.

In the case of slow drift, electron diffusion becomes important, and this can lead to the coalescence of two clusters or the breakup of many-electron clusters into individual electrons. (We recall that in argon 80% of the clusters consist of single electrons.[76]) Calculation showed that in the case of very good space resolution $\rho_x \leq 50$ μm ($\tau \leq 5$ nsec) effective counting of separate electrons within clusters is ensured, so that $\bar{N}_c > N_1$. As a result, the distribution of the counts becomes broader and approaches the distribution of the total ionization. It is interesting to note that $\bar{N}_c = N_1$ for $\rho_x \approx 50$ μm, and the distribution of the counts is of Poisson type. If the resolution is less good ($\rho_x > 50$ μm), the distribution becomes somewhat narrower, but the mean number $\bar{N}_c$ of counts decreases.[76] The minimal value of the relative rms deviation $\sigma_c(\rho_x)$ of the distribution N_c in the presence of diffusion ($\sigma_d = 200$ μm) corresponds to $\rho_x \approx 100$ μm.

Lapique and Piuz[76] calculated the number n of layers of the identifier needed to distinguish between a proton and a K meson with given confidence:

$$S_n(p, K) = [\bar{N}_c(p) - \bar{N}_c(K)]/\sigma_n, \qquad (54)$$

where $\sigma_n = \sigma_c/\sqrt{n}$. The results of their calculations, which are given in Fig. 40a for $S_n(p, K) = 2$, show the reliability with which one can identify p and K at $p = 5$–20 GeV/c in an instrument of length 1 m when $l = 1$ cm and $\rho_x \leq 100$ μm. An increase in the length of the identifier to 3 m raises the upper limit of the interval of momenta to about 50 GeV/c. It should be noted that the chosen

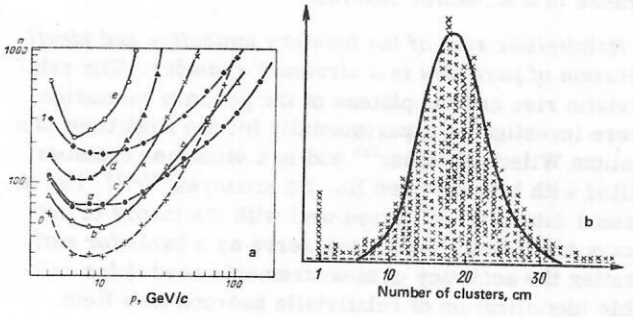

FIG. 40. Number n of layers needed to separate protons and K mesons with confidence $S_n(p, K) = 2$ in argon, $l = 10$ mm (Ref. 76) (a) and distribution of the number of clusters from part of a track of length 24 mm, $l = 35$ mm, $v_d = 12$ mm/μsec (b): the curves a, b, c, d, and e correspond to the cluster counts for $\rho_x = 20$, 50, 100, 150, 200 μm and $\sigma_d = 200$ μm; 1 is the measurement of the probable ionization, and 0 is the cluster count for $\rho_x = 0$, $\sigma_d = 200$ μm.

reliability of identification $S_\pi(p,K)=2$ is not high. For comparison, we have also shown in Fig. 40a the dependence of the number of layers needed to identify p and K using measurement of the total ionization.

As we have already said, the efficiency of particle identification is determined not only by the amplitude resolution of the instrument but also by the relativistic rise R_1 of the primary ionization. It follows from Fig. 3 and Tables I and III that the relativistic rise of the primary ionization in argon ($R_1=1.38$) is appreciably less than the rise in the probable energy loss ($R=1.59$), and the primary ionization is already saturated at $\gamma \approx 200$. Despite this, because of the symmetry of the distribution of the primary ionization in the case of good space resolution ($\rho_x \leq 100$ μm) a drift chamber intended for cluster counting requires fewer layers than in the case of measurement of the ionization energy loss.

The number of layers can also be further reduced by increasing their length l. It was shown in Ref. 217 that a symmetric distribution of the number of clusters, which can be approximated by a Poisson distribution, can be obtained for $l \leq 35$ mm (see Fig. 40b).

The measured number of clusters at the ionization minimum ($\gamma=4$), $\bar{N}_c=12.3$ cm^{-1},[216] does not correspond to the calculated value 20 cm^{-1} (Ref. 76) for $\rho_x=100$ μm and $\sigma_d=200$ μm. This can be explained by the insufficient efficiency of counting of the single-electron clusters. On the other hand, the calculations of Ref. 217 showed that for $\bar{N}_c=12$ the counting losses due to the dead time of the electronics are unimportant. The measured relativistic rise $R_c=1.2$ in the number of electrons is not large, but it agrees with the calculated value for $\rho_x=120$ μm.

In chambers with slow electron drift there are difficulties due to the high gas gain needed for the detection of individual electrons. Therefore, one must contend with a spread of the pulse heights and the accumulation of positive space charge near the position at which the electrons are collected at the wire. However, this effect is strongly reduced if there is even a small inclination of the track to the wire.

The existing drift chambers for cluster counting (Refs. 4, 114, 216, and 217) are to be regarded as models for investigation of the method itself. Before an identifer based on cluster counting is constructed, it is necessary to study and optimize: 1) the time resolution of the electronics; 2) the electron drift velocity; 3) the gas amplification; 4) the thickness and number of layers; 5) the gas mixture and its pressure.

Compared with the method in which the ionization energy loss is measured, the cluster-counting method has the following advantages: shorter length of the identifier and lower cost of the electronics channels, simplicity, reliability, reduction in the information flux, a decrease in the memory time, and an increase in the admissible load. Among the shortcomings of the method are the large number of electronics channels, the poorer space resolution, and the impossibility of identifying particles with high ($\gamma \geq 200$) momenta.

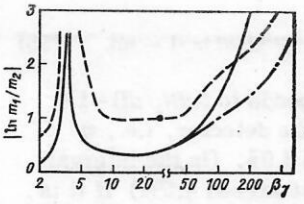

FIG. 41. Dependence of the calculated resolution of two particles with masses m_1 and m_2 (in units of the half-width of the distribution of the mass measurement) on $\beta\gamma$ in 1 m of argon at $P=1$ atm (Ref. 12); the continous curve corresponds to measurement of the primary ionization, and the broken curve to measurement of the total ionization (ISIS-I); the chain curve corresponds to measurement of the primary ionization with weighting of the clusters.

The calculated mass resolution of the particles [see (53)], given ideal measurements of the primary and total ionizations, i.e., without experimental errors and instrumental effects, is shown in Fig. 41. In the range $\gamma=4$–100, measurement of the primary ionization ensures much better separation of the particles than measurement of the total ionization. The most reliable results are obtained by simultaneous use of both methods, i.e., simultaneous measurement of the number and charge of the clusters.

Measurement of primary ionization based on the efficiency of gas-discharge detectors and the formation time of a spark discharge

Measurement of the primary ionization based on the efficiency of a gas-discharge detector. This method has been used to study the ionizing capacity of particles since the thirties.[219-223] Low-efficiency Geiger counters were used to make detailed measurements of the primary ionization in gases in the region of the minimum and the start of the logarithmic rise.[224,225] The method is based on the fact that whereas a single free electron is sufficient to cause a detector response, the detector efficiency η (the probability of a response) depends on the primary ionization produced in the gas by the charged particle.

By virtue of the random nature of the collisions of the particle in the gas,

$$\eta = 1 - \exp\left[-l\,(dN_1/dl)_{P,T}\right], \tag{55}$$

where $l(dN_1/dl)_{P,T}$ corresponds to the number of primary electrons in a detector of length l (cm) at pressure P (atm) and temperature T (°K). Under normal conditions, the primary specific ionization in the gas is

$$(dN_1/dl) = -[\ln(1-\eta)]/Pl\,(273/T). \tag{56}$$

The standard error of a measurement of the efficiency in n measurements

$$\langle\delta\eta\rangle = [\eta\,(1-\eta)/n]^{1/2} \tag{57}$$

corresponds to a binomial distribution in accordance with two possibilities: response and nonresponse of the detector. At the same time, the relative error in the measurement of the primary ionization is

$$\langle \delta\,(dN_1/dl)\rangle / dN_1/dl$$
$$= -\{\exp[-\ln(1-\eta)] - 1\}^{1/2}/[n^{1/2}\ln(1-\eta)|. \qquad (58)$$

The maximal accuracy corresponds to $l(dN_1/dl) = 1.6$ pairs of ions in the volume of the detector, i.e., $\eta = 0.8$, and for $n = 10^3$ it reaches 3.9%. (In the interval $0.5 < \eta < 0.95$, the error does not exceed 4.6%.) If it is necessary to identify a particle, the optimal value of η can differ slightly from 0.8.[226]

At the present time, low-efficiency counters have been replaced by controlled pulsed detectors: neon discharge tubes,[227,228] and also narrow-gap spark[168,229-233] and projection[234] chambers with large useful volume; besides the primary ionization, these also permit measurement of the track coordinates. Optimal efficiency of a spark chamber is ensured by a reduction in the size of the spark gap or a decrease in the gas pressure. In discharge tubes, it is achieved by increasing the delay of the high-voltage pulse to $\tau_d = 10$–40 μsec, so that they are sensitive to the total rather than the primary ionization.[235]

To reduce the loss of ionization electrons by diffusion to the electrodes of the spark chamber during the delay time τ_d, and also because of electron drift on the leading edge of the high-voltage pulse and to eliminate secondary electron emission, it is better to use not continuous electrodes but rather wire electrodes with transparency $\geq 90\%$.[168,232-234] The information is extracted by photography,[230,234] by means of a photomultiplier,[168,231,232] or by the magnetostriction method.[231,233] Purity and constancy of the gas composition are achieved either by flushing the gas through the chamber or by continuous purification.[168,231,232] The existence of a plateau of the efficiency with respect to the amplitude of the high-voltage pulse indicates that one free electron in the gas is sufficient for the development of a spark discharge.[168]

When the measurement of the primary ionization is based on the efficiency of a spark chamber, it is necessary to introduce corrections for the diffusion of electrons[168,231] and secondary electron and atom collisions in the gas (see above). However, these processes do not affect the relative relativistic rise of the measured primary ionization[232] or, therefore, the reliability of particle identification. Note that, in contrast to streamer chambers, such a method is suitable even for gases with a large coefficient of electron diffusion.

Particles are identified using the efficiency of a multilayer detector containing low-efficiency counters,[223] discharge tubes,[228] or spark chambers[229,233] in cosmic-ray and accelerator experiments (Fig. 42). To obtain an accuracy of about 3%, which is needed for the reliable identification of hadrons in the region of logarithmic rise of the primary ionization, a detector with $n \gtrsim 10^3$ layers is needed.[81] It can be based on not only spark chambers but also discharge tubes, and also proportional chambers working in the high-current regime.[236] Such a detector does not require complicated electronics, since it is here not necessary to measure the pulse heights. However, the need to have 10^3 or more layers seriously complicates its preparation, and

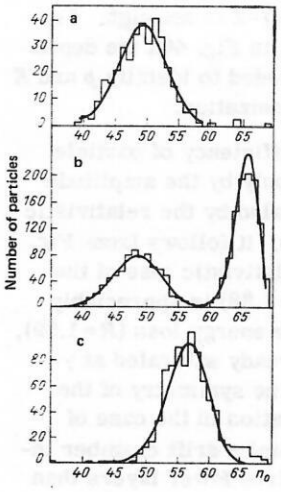

FIG. 42. Distributions with respect to the number n_0 of layers that respond in a 69-layer spark detector filled with He + 0.7% N_2: a) π^-, $p = 0.5$ GeV/c; b) π^+, $p = 0.5$ GeV/c; c) e^-, $p = 0.25$–2.5 GeV/c; the smooth curves are the binomial distributions that approximate the experimental histograms.[233]

as yet there are no examples of the construction of such multilayer systems.

Possibilities of identifying particles by means of the discharge formation time in a spark chamber. In high-energy physics experiments, multigap spark chambers are frequently used to determine particle coordinates. Measurement of the spark formation time, which can be determined from the sharp change in the potential on the the electrodes of the spark chamber (Fig. 43), can give additional information about the ionizing capacity of the particle.[151,237,238] Indeed, the spark is formed by virtue of the development and merging of avalanches that grow on the clusters of ionization electrons left by the charged particle in the gas. The number of such avalanches is greater, and the distances between them shorter, the higher the density of the charges in the gap of the spark chamber. Therefore, the formation time τ_f of the spark discharge, which is basically determined by the development and merging of the avalanches into streamers, which then coalesce into a single conducting plasma channel, decreases with increasing ionizing capacity of the particle. It is to be expected that, as in a streamer chamber, this effect will be determined by

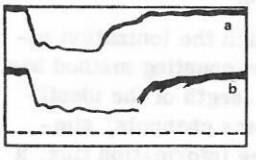

FIG. 43. Oscillograms of voltage pulses in a spark chamber filled with He of high purity; $\mathscr{E} = 8$ kV/cm; $l = 1.5$ cm: a) α particles; b) β particles. The marks measure 10 nsec.[239] The trailing edges of the pulses correspond to the development of spark breakdown.

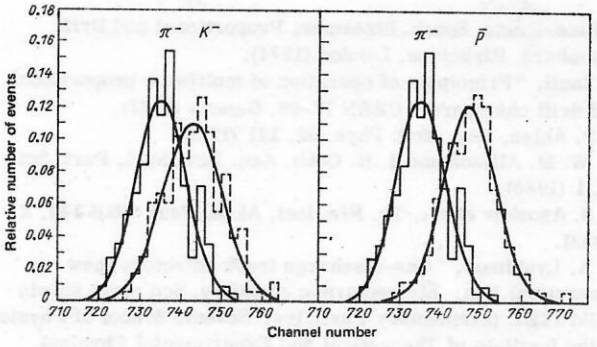

FIG. 44. Distributions of averaged values τ_f of the formation time of a spark discharge in a 30-layer spark chamber ($l=1$ cm) filled with a He + Ne mixture. The areas of the histograms are normalized to 1. The smooth curves are Gaussian distributions that approximate the experimental histograms.[237]

the primary ionization when $\tau_d < 1$ μsec and by the total ionization when $\tau_d \gg 1$ μsec.

For the same length l of the spark gap, the spark formation time depends on the gas composition and on the amplitude U of the high-voltage pulse. Therefore, these must be kept constant to a high accuracy ($\delta U/U \leq 0.5\%$). The values of τ_f for α and β particles with energy 5 MeV and approximately 2 MeV for $l=1.5$ cm and $\mathscr{E}=8$ kV/cm in helium are, respectively, 70 and 90 nsec, while in neon they are 40 and 55 nsec.[239] The fluctuations in the spark formation time for $l=1.9$ cm and $\mathscr{E}=7$ kV/cm for α and β particles in helium reach approximately 2.5 and 6 nsec, respectively,[240] and decrease with increasing l.[241]

Because of the weak dependence of τ_f on dN_1/dl, the identification of particles using the spark formation time is possible only if multiple measurements are made, i.e., in multigap spark chambers. As an example, Fig. 44 shows the distributions of the averaged values of τ_f in a 30-gap spark chamber.[237] (The current pulses from each layer are summed by means of a resistor, and the duration of the resulting voltage pulse is measured by means of an ADC.)

In the 6-gap helium spark spectrometer ($l=3$ cm) of Ref. 242 all the electrodes are connected in a wave line, so that a discharge in one of the gaps raises the potential in the others and accelerates their breakdown. Thus, the duration of the resulting pulse approaches the shortest value of τ_f for an individual spark gap. In this experiment, an accuracy in the measurement of τ_f of about 40% was achieved.

Considering the possibility for identifying individual relativistic particles by this method, one must bear in mind the need to reduce the error of the measurements of τ_f by an order of magnitude (which requires increasing the number of layers by two orders of magnitude). Nevertheless, even with a small number of layers of the spark chamber, measurement of the discharge formation time makes it possible to identify individual particles that differ strongly in their ionizing capacity.[241]

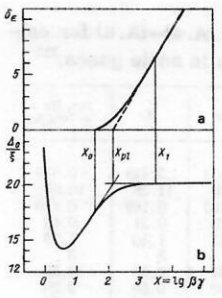

FIG. 45. Dependence of the correction for the density effect (a) and the probable energy loss (b) on $X=\log\beta\gamma$ in a 0.9 Ar + 0.1 CH_4 mixture ($l=2.3$ cm, $P=10.5$ atm).[63]

APPENDIX: CALCULATION OF THE IONIZATION ENERGY LOSS AND THE PRIMARY IONIZATION WITH ALLOWANCE FOR THE POLARIZATION OF THE MEDIUM[9)]

The specific mean, specific restricted, and probable ionization energy losses of relativistic particles are given, respectively, by the expressions (5), (6), and (21), which include a correction δ_E for the density effect of the medium. A simple way of calculating this correction was proposed by Sternheimer[6,243,244] and was developed in Ref. 18. In accordance with Refs. 243 and 244, δ_E can be approximated by the expressions

$$\delta_E = \begin{cases} 0 & \text{for } X < X_0; \\ 4.606X + C + a(X_1 - X)^m & \text{for } X_0 < X < X_1; \\ 4.606X + C & \text{for } X > X_1. \end{cases} \quad \text{(A.1)}$$

Here

$$X = \lg\beta\gamma;\ m=3;\ C = -2\ln(I/\hbar\omega_p) - 1;\quad a = -(C + 4{,}606X_0)/(X_1 - X_0)^m, \quad \text{(A.2)}$$

and the meaning of X_0 and X_1 is explained in Fig. 45. Calculations in accordance with these expressions agree to within 2% (on the average, even to within 1%) with more accurate calculations based on data on the oscillator strengths and decelerating capacity of the material.

The parameters X_0, X_1, and a are given in Table XIV.

TABLE XIV. Parameters of Eq. (A.1) for calculating the correction for the polarization of the medium in the calculation of the ionization energy loss.[18]

State of the matter	I, eV	$\lvert C\rvert$	X_0	X_1
Condensed	<100	<3.681	0.2	2.0
		$\geqslant 3.681$	$0.3261\lvert C\rvert - 1$	2.0
	$\geqslant 100$	<5.215	0.2	3.0
		$\geqslant 5.215$	$0{,}3261\lvert C\rvert - 1.5$	3.0
Gaseous (1 atm, 0°C)		<10.0	1.6	4.0
		$10.0 \leqslant \lvert C\rvert < 10.5$	1.7	4.0
		$10.5 \leqslant \lvert C\rvert < 11.0$	1.8	4.0
		$11.0 \leqslant \lvert C\rvert < 11.5$	1.9	4.0
		$11.5 \leqslant \lvert C\rvert < 12.25$	2.0	4.0
		$12.25 \leqslant \lvert C\rvert < 13.804$	2.0	5.0
		$\lvert C\rvert \geqslant 13.804$	$0.326\lvert C\rvert - 2.5$	5.0

[9)] We here adopt the notation generally employed in the calculation of the correction for the density effect of the medium. Some of the symbols have a meaning different from the one with which they are used in the present review.

TABLE XV. Parameters of Eqs. (3) and (A.4)–(A.6) for calculation of the specific primary ionization in noble gases.[232]

Gas	He	Ne	Ar	Kr	Xe	30% He + 70% Ne
A_1, cm^{-1} · atm^{-1}	0.244	0.844	1.828	2.551	3.448	0.679
A_2	11.64	10.89	11.45	11.30	11.28	10.98
r	0.161	0.171	0.164	0.167	0.169	0.170
y	0.39	0.42	0.31	0.25	0.31	0.42
Y_0	1.88	1.31	1.50	1.47	1.40	1.79
Y_1	3	3	3	3	3	3
$-B$	10.66	11.42	9.36	9.47	9.36	11.35
b	1.50	2.53	0.78	0.89	0.89	2.20
d	2.56	1.44	2.82	2.61	2.53	1.79

For gases with density $\rho = \zeta\rho_0$, where ρ_0 is the density under normal conditions [for ideal gases, $\zeta = P/(T/273)$],

$$\left.\begin{array}{l} X_0(\zeta) = X_0 - (1/2)\lg\zeta;\ X_1(\zeta) = X_1 - (1/2)\lg\zeta; \\ a(\zeta) = a;\ C(\zeta) = C + 2.303\lg\zeta. \end{array}\right\} \quad \text{(A.3)}$$

The correction δ_{N_1} for the polarization of the medium, which occurs in the expression (3) for the specific primary ionization of a gas by relativistic particles, can be calculated by means of similar expressions[17, 232, 245]:

$$\delta_{N_1} = \begin{cases} 0 & \text{for } Y \leqslant Y_0; \\ 4.606Y + B + b(Y_1 - Y)^d & \text{for } Y_0 \leqslant Y \leqslant Y_1; \\ 4.606Y + B & \text{for } Y > Y_1. \end{cases} \quad \text{(A.4)}$$

Here, $Y = \log\gamma$; Y_0 and Y_1 are similar to X_0 and X_1, respectively.

The parameters B, d, and b (and also A_1 and A_2) for gases under normal conditions are given in Table XV. At gas density $\rho = \zeta\rho_0$, they can be calculated by means of the relations

$$\left.\begin{array}{l} B(\zeta) = (A_2 - 1) - (dN_1/dl)_{\min}\,[R_{N_1}(\zeta)]/A_1; \\ d(\zeta) = -4.606\,[Y_1(\zeta) - Y_0(\zeta)]/[4.606Y_0 + B(\zeta)]; \\ b(\zeta) = -4.606\,[Y_0(\zeta) + B(\zeta)]/[Y_1(\zeta) - Y_0(\zeta)]. \end{array}\right\} \quad \text{(A.5)}$$

The values of the relativistic rise $R_{N_1}(\zeta)$ and the parameters $Y_0(\zeta)$ and $Y_1(\zeta)$ can be calculated from the corresponding values R_{N_1}, Y_0, and Y_1 under normal conditions by means of the expressions

$$R_{N_1}(\zeta) = R_{N_1} - r\lg\zeta;\ Y_0(\zeta) = Y_0 - 0.45\lg\zeta;\ Y_1(\zeta) = Y_1 - y\lg\zeta. \quad \text{(A.6)}$$

[The values of $(dN_1/dl)_{\min}$ and R_{N_1} are given in Table I, and of Y_0, Y_1, r, and y in Table XV.] The accuracy of the expressions (A.3) in the region of the transition from the logarithmic rise to the plateau of the primary ionization is a few percent.[245]

[1]W. J. Willis, Phys. Today **31**, 32 (1978).
[2]C. W. Fabjan and H. G. Fisher, Preprint EP/80-27, CERN, Geneva (1980).
[3]A. I. Alikhanyan, in: Trudy Mezhdunarodnogo simpoziuma po perekhodnomu izlucheniyu chastits vysokikh énergiĭ (Proc. of the Intern. Symposium on the Transition Radiation of High Energy Particles), Erevan (1977), p. 41.
[4]C. W. Fabian *et al.*, Nucl. Instrum. Methods **185**, 119 (1981).
[5]B. Rossi, High Energy Particles, Prentice-Hall, New York (1952) [Russian translation published by Gostekhteorizdat, Moscow (1955)].
[6]R. M. Sternheimer, "Interaction of radiation with matter," in: Methods of Experimental Physics, Vol. 5A (eds. L. C. L. Yuan and C. S. Wu), Academic Press, New York (1961), pp. 4–55 [Russian translation published by Izd. Inostr. Lit., Moscow (1963), p. 9].
[7]U. Fano, Ann. Rev. Nucl. Sci. **13**, 1 (1963).
[8]A. Crispin and G. N. Fowler, Rev. Mod. Phys. **42**, 290 (1970).
[9]P. Rice-Evans, Spark, Streamer, Proportional and Drift Chambers, Risheleue, London (1974).
[10]F. Sauli, "Principles of operation of multiwire proportional and drift chambers," CERN 77-09, Geneva (1977).
[11]S. P. Ahlen, Rev. Mod. Phys. **52**, 121 (1980).
[12]W. W. M. Allison and J. H. Cobb, Ann. Rev. Nucl. Part. Sci. **30**, 1 (1980).
[13]V. S. Asoskov *et al.*, Tr. Fiz. Inst. Akad. Nauk SSSR **140**, 2 (1983).
[14]V. A. Lyubimov, "Gas-discharge track detectors (new generation)," in: Élementarnye chastitsy. Sed'maya shkola fiziki ITÉF (Elementary Particles. Seventh School of Physics of the Institute of Theoretical and Experimental Physics), No. 2, Atomizdat, Moscow (1980), p. 91.
[15]V. C. Ermilova *et al.*, Nucl. Instrum. Methods **145**, 555 (1977).
[16]E. Fermi, Phys. Rev. **57**, 485 (1940).
[17]V. K. Ermilova *et al.*, Zh. Eksp. Teor. Fiz. **56**, 1608 (1969) [Sov. Phys. JETP **29**, 861 (1969)].
[18]R. M. Sternheimer and R. F. Peierls, Phys. Rev. B **3**, 3681 (1971).
[19]A. V. Alakoz *et al.*, Nucl. Instrum. Methods **124**, 41 (1975).
[20]V. N. Tsytovich, Dokl. Akad. Nauk SSSR, **144**, 310 (1962) [Sov. Phys. Dokl. **7**, 411 (1962)].
[21]G. B. Zhdanov *et al.*, Zh. Eksp. Teor. Fiz. **44**, 1864 (1963) [Sov. Phys. JETP **17**, 1254 (1963)].
[22]P. J. McNulty and F. J. Congel, Phys. Rev. D **1**, 3041 (1970).
[23]J. P. Burq *et al.*, Nucl. Instrum. Methods **187**, 407 (1981).
[24]E. G. Drukarev, Yad. Fiz. **33**, 404 (1981) [Sov. J. Nucl. Phys. **33**, 215 (1981)].
[25]M. I. Dodgoretskiĭ, Dokl. Akad. Nauk SSSR **67**, 631, 823 (1949).
[26]V. M. Kharitonov, Izv. Akad. Nauk SSSR, Ser. Fiz. **17**, 102 (1953).
[27]R. M. Sternheimer, Phys. Rev. **145**, 247 (1966).
[28]P. Dalton and J. E. Turner, Health Phys. **15**, 257 (1968).
[29]L. G. Christophorou, Atomic and Molecular Physics, Wiley, New York (1970).
[30]G. S. Hurst *et al.*, J. Chem. Phys. **42**, 713 (1965).
[31]J. N. Marx and D. R. Nygren, Phys. Today **31**, 46 (1978).
[32]U. Fano, Phys. Rev. **72**, 26 (1947).
[33]G. Charpak, Ann. Rev. Nucl. Sci. **20**, 195 (1970).
[34]V. A. Davidenko *et al.*, Zh. Eksp. Teor. Fiz. **55**, 426 (1968) [Sov. Phys. JETP **28**, 223 (1969)].
[35]L. D. Landau, in: Sobranie trudov (Collected Works), Vol. 1, Nauka, Moscow (1969), p. 482.
[36]P. V. Vavilov, Zh. Eksp. Teor. Fiz. **32**, 920 (1957) [Sov. Phys. JETP **5**, 749 (1957)].
[37]K. Symon, Thesis, Harvard University (1948).
[38]N. Bohr, Philos. Mag. **30**, 581 (1915).
[39]W. Borsch-Supan, J. Natl. Bur. Stand. **B65**, 245 (1961).
[40]J. E. Moyal, Philos. Mag. **46**, 263 (1955).
[41]H. P. Maccabee and P. G. Papworth, Phys. Lett. **A30**, 241 (1969).
[42]D. West, Proc. Phys. Soc. London **66**, 306 (1953).
[43]J. K. Parry, H. D. Rathgeber, and J. L. Rouse, Proc. Phys. Soc. London **66**, 541 (1953).
[44]E. F. Bradley, Proc. Phys. Soc. London **68**, 549 (1953).
[45]E. D. Palmatier, J. T. Meers, and C. M. Askey, Phys. Rev. **97**, 486 (1955).
[46]G. Hall, Can. J. Phys. **37**, 189 (1959).
[47]P. V. Ramana Murthy and G. D. Deemestr, Nucl. Instrum. Methods **56**, 93 (1967).
[48]P. V. Ramana Murthy, Nucl. Instrum. Methods **63**, 77 (1968).
[49]Z. Dimcovsky *et al.*, Nucl. Instrum. Methods **94**, 151 (1971).
[50]S. Parker *et al.*, Nucl. Instrum. Methods **94**, 181 (1971).
[51]F. Harris *et al.*, Nucl. Instrum. Methods **107**, 413 (1973).
[52]D. Jeanne *et al.*, Nucl. Instrum. Methods **111**, 287 (1973).
[53]M. Aderholz *et al.*, Nucl. Instrum. Methods **118**, 419 (1974).
[54]W. W. M. Allison *et al.*, Nucl. Instrum. Methods **119**, 499 (1974).

[55]A. B. Onuchin and V. I. Telnov, Nucl. Instrum. Methods **120**, 365 (1974).
[56]M. L. Cherry *et al.*, Phys. Rev. **100**, 3594 (1974).
[57]J. Fisher *et al.*, Nucl. Instrum. Methods **127**, 525 (1975).
[58]E. A. Kopot' *et al.*, Zh. Eksp. Teor. Fiz. **70**, 387 (1976) [Sov. Phys. JETP **43**, 200 (1976)].
[59]W. W. M. Allison *et al.*, Nucl. Instrum. Methods **133**, 325 (1976).
[60]K. Nagata *et al.*, J. Phys. D **9**, 1907 (1976).
[61]I. Lehraus *et al.*, Nucl. Instrum. Methods **153**, 437 (1978).
[62]N. Hasebe *et al.*, Nucl. Instrum. Methods **155**, 491 (1978).
[63]A. H. Walenta *et al.*, Nucl. Instrum. Methods **161**, 45 (1979).
[64]K. Nagata *et al.*, Nucl. Instrum. Methods **172**, 601 (1980).
[65]J. M. Cobb, W. W. M. Allison, and J. H. Bunch, Nucl. Instrum. Methods **133**, 315 (1976).
[66]C. Rubbia, Preprint NP 70-25, CERN, Geneva (1970).
[67]O. Blunck and S. Leisegang, Z. Phys. **128**, 500 (1950).
[68]O. Blunck and K. Westphall, Z. Phys. **130**, 641 (1951).
[69]V. A. Chechin and V. C. Ermilova, Nucl. Instrum. Methods **136**, 551 (1976).
[70]R. Talman, Nucl. Instrum. Methods **159**, 189 (1979).
[71]V. A. Soloshchenko, Preprint 114 [in Russian], Institute of Theoretical and Experimental Physics, Moscow (1980).
[72]H. Bichsel, Phys. Rev. B **1**, 2584 (1970).
[73]A. Shulek *et al.*, Yad. Fiz. 4, 564 (1966) [Sov. J. Nucl. Phys. 4, 400 (1967)].
[74]K. A. Ispirian, A. T. Margarian, and A. M. Zverev, Nucl. Instrum. Methods **117**, 125 (1974).
[75]A. R. Clark *et al.*, Proposal for PEP Facility Based on Time Projection Chamber, PEP Experiment No. 4 (1976).
[76]F. Lapique and F. Piuz, Nucl. Instrum. Methods **175**, 297 (1980).
[77]A. Alikhanian, A. Alikhanov, and S. Nikitin, J. Phys. **9**, 167 (1945).
[78]S. Ya. Nikitin, Zh. Eksp. Teor. Fiz. **18**, 577 (1948).
[79]J. Becker *et al.*, Proc. Phys. Soc. London Sect. A **65**, 437 (1952).
[80]G. P. Eliseev, V. K. Kosmachevskiĭ, and V. A. Lyubimov, Dokl. Akad. Nauk SSSR **90**, 995 (1953).
[81]A. I. Alikhanov, V. A. Lubimov, and G. P. Eliseev, in: Proc. of the Intern. Symposium on High Energy Physics, Vol. 2, CERN, Geneva (1956), p. 87.
[82]L. P. Kotenko, Izv. Akad. Nauk SSSR, Ser. Fiz. **19**, 525 (1955).
[83]A. I. Anoshin *et al.*, Izv. Akad. Nauk SSSR, Ser. Fiz. **36**, 1640 (1972).
[84]G. L. Bashindzhagyan, Kand. dissertatsiya (Candidate's Dissertation), Institute of Nuclear Physics, Moscow State University (1980).
[85]H. Cramér, Mathematical Methods of Statistics, Princeton University Press (1946) [Russian translation published by Izd. Inostr. Lit., Moscow (1948)].
[86]W. A. Oran, Nucl. Instrum. Methods **97**, 151 (1971).
[87]G. Igo and R. M. Eisberg, Rev. Sci. Instrum. **25**, 450 (1954).
[88]G. L. Bashindzhagyan and N. B. Sinev, Prib. Tekh. Eksp. No. 1, 59 (1977).
[89]G. L. Bashindzhagyan, L. I. Sarycheva, and N. B. Sinev, in: Proc. of the 15th Intern. Cosmic Ray Conf., Vol. 9 (1977), p. 185.
[90]W. W. M. Allison *et al.*, Nucl. Instrum. Methods **163**, 331 (1979).
[91]B. F. Wadsworth *et al.*, IEEE Trans. Nucl. Sci. **26**, 120 (1979).
[92]A. I. Babaev *et al.*, Preprint 103 [in Russian], Institute of Theoretical and Experimental Physics, Moscow (1978).
[93]Yu. A. Budagov *et al.*, UKJF 80-30, Bratislava (1980).
[94]A. V. Vishnevskiĭ *et al.*, Preprint 53 [in Russian], Institute of Theoretical and Experimental Physics, Moscow (1979).
[95]W. Farr *et al.*, Nucl. Instrum. Methods **156**, 283 (1978); H. Drumm *et al.*, IEEE Trans. Nucl. Sci. **26**, 81 (1979).
[96]D. Cockerill *et al.*, Nucl. Instrum. Methods **176**, 159 (1980).
[97]H. Hasmann *et al.*, Preprint DESY-148 (1978).
[98]C. Rubbia *et al.*, Preprint CERN/SPSC/78-06 (1978).
[99]J. Va'vra and D. Rust, IEEE Trans. Nucl. Sci. **28**, 416 (1981).
[100]R. Ehrlich *et al.*, IEEE Trans. Nucl. Sci. **28**, 421 (1981).
[101]M. Boerner *et al.*, Nucl. Instrum. Methods **176**, 151 (1980).
[102]R. Davies-White *et al.*, Nucl. Instrum. Methods **160**, 227 (1979).
[103]W. De Boer *et al.*, Nucl. Instrum. Methods **176**, 167 (1980).
[104]K. Winter, in: Proc. of the Intern. Conf. on Experimentation at LEP, Uppsala (1980).
[105]E. Gabathuler, in: Proc. of the Intern. Conf. on Experimentation at LEP, Uppsala (1980).
[106]I. Lehraus, R. Matthewson, and W. Tejessy, in: Proc. of the Intern. Conf. on Experimentation at LEP, Uppsala (1980).
[107]A. Wagner, in: Proc. of the Intern. Conf. on Experimentation at LEP, Uppsala (1980).
[108]P. Lazeyras *et al.*, IEEE Trans. Nucl. Sci. **NS-26**, 89 (1979).
[109]W. W. M. Allison *et al.*, Preprint CERN/EP/EHS/PH 78-10, CERN (1978).
[110]Proc. of the Wire Chamber Conf., Vienna (1978), Part IV - Cylindrical Chambers and Drift Tubes; Nucl. Instrum. Methods **156**, 227 (1978); **176**, 151 (1978).
[111]J. Heintze, Nucl. Instrum. Methods **156**, 227 (1978).
[112]D. Francher *et al.*, Nucl. Instrum. Methods **161**, 383 (1979).
[113]T. Ludlam *et al.*, IEEE Trans. Nucl. Sci. **28**, 439 (1981).
[114]A. H. Walenta, IEEE Trans. Nucl. Sci. **26**, 73 (1979).
[115]J. L. Pack and A. V. Phelps, J. Chem. Phys. **45**, 4316 (1966).
[116]A. Breskin and N. Trautner, Nucl. Instrum. Methods **134**, 35 (1976).
[117]R. Janik *et al.*, Nucl. Instrum. Methods **178**, 71 (1980).
[118]M. Barranko Luque *et al.*, Nucl. Instrum. Methods **176**, 175 (1980).
[119]V. M. Golovayuk *et al.*, Nucl. Instrum. Methods **140**, 259 (1977).
[120]H. Frehse *et al.*, Nucl. Instrum. Methods **156**, 97 (1978).
[121]A. Breskin, G. Charpak, *et al.*, Nucl. Instrum. Methods **143**, 29 (1977).
[122]D. Friedrich *et al.*, Nucl. Instrum. Methods **158**, 81 (1979).
[123]F. Sauli, Nucl. Instrum. Methods **156**, 147 (1978).
[124]G. Charpak and F. Sauli, Nucl. Instrum. Methods **162**, 405 (1979).
[125]N. A. Filatova *et al.*, Nucl. Instrum. Methods **143**, 17 (1977).
[126]Yu. V. Zanevskiĭ, Provolochnye detektory élementarnykh chastits [Wire Detectors of Elementary Particles), Atomizdat, Moscow (1978)].
[127]J. Fischer *et al.*, Nucl. Instrum. Methods **136**, 19 (1976).
[128]C. W. Fabjan *et al.*, Nucl. Instrum. Methods **156**, 267 (1978).
[129]V. Radeka and P. Rehak, IEEE Trans. Nucl. Sci. **26**, 225 (1978).
[130]H. G. Fischer and J. Pich, Nucl. Instrum. Methods **100**, 515 (1972).
[131]L. Criegee *et al.*, in: Proc. of the Intern. Meeting on Proportional and Drift Chambers, Dubna (1975); Preprint D13 [in English], JINR, Dubna (1964), p. 76.
[132]G. Charpak *et al.*, Nucl. Instrum. Methods **167**, 455 (1979).
[133]M. Atac and J. Urish, Nucl. Instrum. Methods **156**, 163 (1978).
[134]Short Description of D. T. R. System, CERN (1980).
[135]C. B. Brooks, P. D. Shield, and W. W. M. Allison, Nucl. Instrum. Methods **156**, 297 (1978).
[136]W. Farr and J. Heintze, Nucl. Instrum. Methods **156**, 301 (1978).
[137]L. M. Soroko, Fiz. Elem. Chastits At. Yadra **10**, 1038 (1979) [Sov. J. Part. Nucl. **10**, 412 (1979)].
[138]Yu. R. Nosov and V. A. Shilin, Poluprovodnikovye pribory s zaryadovoĭ svyaz'yu (Semiconductor Charge-Coupled Devices), Sov. Radio, Moscow (1976).
[139]Ch. Séquin and M. F. Tompsett, Charge Transfer Devices, Supplement 8 to Advances in Electronics and Electron Physics, Academic Press, New York (1975) [Russian translation published by Mir, Moscow (1978)].
[140]D. L. Fancher *et al.*, IEEE Trans. Nucl. Sci. **26**, 212 (1979).

[141]H. J. Hilke, Pulse Shaping for the TPC, TPC Meeting, LBL, Berkeley (1978).
[142]B. M. Gordon, IEEE Trans. Circuits Syst. **23**, 391 (1978); Electronics **51**, 33 (1978).
[143]M. Calvetti *et al.*, Nucl. Instrum. Methods **176** (1980).
[144]B. Hallgren and H. Werveij, IEEE Trans. Nucl. Sci. **27**, 333 (1980).
[145]T. Lingjaerde and D. Marland, Preprint CERN/DD/77-8, CERN (1977).
[146]V. A. Mikhaĭlov, V. N. Roĭnishvili, and G. E. Chikovani, Zh. Eksp. Teor. Fiz. **45**, 819, 1282 (1963) [Sov. Phys. JETP **18**, 562, 879 (1964)].
[147]B. A. Dolgoshein and B. I. Luchkov, Zh. Eksp. Teor. Fiz. **46**, 392 (1964) [Sov. Phys. JETP **19**, 266 (1964)].
[148]V. V. Bovin *et al.*, Prib. Tekh. Eksp. No. 3, 19 (1957).
[149]C. Ballario *et al.*, Nuovo Cimento **19**, 1142 (1961).
[150]M. I. Daĭon *et al.*, Iskrovaya kamera (The Spark Chamber), Atomizdat, Moscow (1967).
[151]O. C. Allkofer, Spark Chambers, Verlag Karl Thiemig KG, Munich (1969).
[152]Yu. A. Shcherbakov, in: Mezhdunarodnaya konferentsiya po apparature v fizike vysokikh énergiĭ, Dubna, 1970 (Intern. Conf. on Apparatus in High Energy Physics, Dubna, 1970), Vol. 1, Dubna (1971), p. 323.
[153]S. V. Somov, Strimernaya kamera v éksperimentakh na uskoritelyakh (Streamer Chambers in Accelerator Experiments), Moscow Engineering Physics Institute (1975).
[154]A. A. Vorob'ev, N. S. Rudenko, and V. I. Smetanin, Tekhnika iskrovykh kamer (Technology of Spark Chambers), Atomizdat, Moscow (1978).
[155]J. Sandweiss, Phys. Today **31**, 40 (1978).
[156]P. Lecoq *et al.*, Avalanche Chamber at LEP, SSG/II/5/27-3-1979, Geneva (1979).
[157]B. A. Dolgoshein, B. I. Luchkov, and B. U. Rodionov, Preprint A-10 [in Russian], P. N. Lebedev Physics Institute, Moscow (1964).
[158]E. Gygi and F. Shneider, Preprint 66-14, CERN, Geneva (1966).
[159]T. L. Asatiani *et al.*, Pis'ma Zh. Eksp. Teor. Fiz. **6**, 571, 684 (1967) [JETP Lett. **6**, 83, 171 (1967)].
[160]V. Davidenko, B. Dolgoshein, and S. Somov, Nucl. Instrum. Methods **75**, 277 (1969).
[161]R. W. Morrison, in: Streamer Chamber Technology, ANL-8055, Argonne National Laboratory (1972), p. 150.
[162]V. A. Davidenko, B. A. Dolgoshein, and S. V. Somov, Zh. Eksp. Teor. Fiz. **56**, 3 (1969) [Sov. Phys. JETP **29**, 1 (1969)].
[163]V. A. Davidenko, B. A. Dolgoshein, and S. V. Somov, Zh. Eksp. Teor. Fiz. **55**, 435 (1968) [Sov. Phys. JETP **28**, 227 (1969)].
[164]V. A. Davidenko *et al.*, Zh. Eksp. Teor. Fiz. **57**, 84 (1969) [Sov. Phys. JETP **30**, 49 (1970)].
[165]V. A. Davidenko *et al.*, in: Mezhdunarodnaya konferentsiya po apparature v fizike vysokikh énergiĭ, Dubna, 1970 (Intern. Conf. on Apparatus in High Energy Physics, Dubna 1970), Vol. 1, Dubna (1971), p. 339.
[166]V. A. Davidenko *et al.*, Zh. Eksp. Teor. Fiz. **58**, 130 (1970) [Sov. Phys. JETP **31**, 74 (1970)].
[167]A. Kanoisky and N. Shoen, Rev. Sci. Instrum. **40**, 921 (1969).
[168]V. S. Asoskov *et al.*, Zh. Eksp. Teor. Fiz. **73**, 146 (1977) [Sov. Phys. JETP **46**, 75 (1977)].
[169]G. L. Braglia, G. M. de Munari, and G. Mambriani, Comit. Naz. Nucl. RT/Fi (65)60, Rome (1965).
[170]L. P. Kotenko *et al.*, Nucl. Instrum. Methods **54**, 119 (1967).
[171]E. W. McDaniel, Collision Phenomena in Ionized Gases, Wiley, New York (1964) [Russian translation published by Mir, Moscow (1967)].
[172]A. von Engel, Ionized Gases, 2nd Ed., Clarendon Press, Oxford (1965) [Russian translation of 1st Ed. published by Fizmatgiz, Moscow (1959)].
[173]J. B. Hasted, Physics of Atomic Collisions, Butterworths, London (1964) [Russian translation published by Mir, Moscow (1965)].
[174]B. M. Smirnov, Atomnye stolknoveniya i élementarnye protsessy v plazme (Atomic Collisions and Elementary Processes in Plasmas), Atomizdat, Moscow (1968).
[175]N. Z. Anisimova *et al.*, Prib. Tekh. Eksp. No. 2, 70 (1971).
[176]M. I. Daĭon *et al.*, Prib. Tekh. Eksp. No. 5, 64 (1970).
[177]N. Z. Anisimova *et al.*, Zh. Eksp. Teor. Fiz. **63**, 21 (1972) [Sov. Phys. JETP **36**, 10 (1973)].
[178]V. Eckardt *et al.*, Nucl. Instrum. Methods **143**, 235 (1977).
[179]V. Eckardt and A. Ladage, in: Mezhdunarodnaya konferentsiya po apparature v fizike vysokikh énergiĭ, Dubna, 1970 (Intern. Conf. on Apparatus in High Energy Physics, Dubna 1970), Vol. 1, Dubna (1971), p. 335.
[180]V. A. Mikhaĭlov and N. S. Il'in, Prib. Tekh. Eksp. No. 3, 204 (1969).
[181]V. Eckardt, DESY 70/60, Hamburg (1970).
[182]T. V. Allaby *et al.*, in: Materialy soveshchaniya po besfil'movym iskrovym i strimernym kameram (Proc. of the Symposium on Filmless Spark and Streamer Chambers), JINR 13-4527, Dubna (1969), p. 51.
[183]G. Bohm *et al.*, in: Streamer Chamber Technology, ANL-8055, Argonne National Laboratory (1972).
[184]K. Eggert, W. Gurich, and E. Smetan, in: Proc. of the Intern. Conf. on Instrumentation for High Energy Physics, Frascati (1973), p. 181.
[185]K. Eggert, PITHA-74, Aachen (1974).
[186]K. Eggert *et al.*, Nucl. Instrum. Methods **126**, 477 (1975).
[187]F. Rohrbach, Nucl. Instrum. Methods **141**, 229 (1977).
[188]M. Basilie *et al.*, CERN 80-1, Geneva (1980).
[189]D. Kiss, Fiz. Elem. Chastits At. Yadra **10**, 551 (1979) [Sov. J. Part. Nucl. **10**, 214 (1979)].
[190]J. Allan *et al.*, in: Experiments at CERN in 1980, CERN, Geneva (1980), p. UA5.
[191]A. G. Kalimov *et al.*, Preprint 407 [in Russian], Leningrad Institute of Nuclear Physics (1980).
[192]A. G. Kalimov *et al.*, Pis'ma Zh. Eksp. Teor. Fiz. **30**, 460 (1979) [JETP Lett. **30**, 429 (1979)].
[193]A. G. Kalimov *et al.*, Preprint 518 [in Russian], Leningrad Institute of Nuclear Physics (1979); A. I. Budzyak *et al.*, Preprints 1-80-299, 1-80-303 [in Russian], JINR, Dubna (1980).
[194]K.-P. Glasnek and G. M. Kadykov, Preprint 10-10923 [in Russian], JINR, Dubna (1977).
[195]M. Basilie *et al.*, in: Intern. Conf. on Experimentation at LEP, Uppsala (1980).
[196]M. V. Stabnikov and M. A. Tombak, in: Mezhdunarodnaya konferentsiya po apparature v fizike vysokikh énergiĭ, Dubna, 1970 (Intern. Conf. on Apparatus in High Energy Physics, Dubna, 1970), Vol. 1, Dubna (1971), p. 382.
[197]M. V. Stabnikov and M. A. Tombak, Preprint 497 [in Russian], Leningrad Institute of Nuclear Physics (1979).
[198]A. G. Kalimov *et al.*, Zh. Tekh. Fiz. **3**, 1057 (1977) [Sov. Phys. Tech. Phys. **3**, 434 (1977)].
[199]M. F. Lomanov and B. V. Chirikov, Prib. Tekh. Eksp. No. 5, 22 (1957).
[200]M. Blau, in: Methods of Experimental Physics, Vol. 5, Part A (eds. L. C. L. Yuan and C. S. Wu), Academic Press, New York (1961), p. 208 [Russian translation published by Izd. Inostr. Lit., Moscow (1963)].
[201]F. Shneider, CERN ISR-GS/69-2, Geneva (1969).
[202]C.-P. Glasneck and G. Peter, PHE 75-9, Berlin-Zeuthen (1975).
[203]S. V. Somov, Dissertatsiya (Dissertation), Moscow Engineering Physics Institute (1968).
[204]A. V. Petrakov and V. M. Kharitonov, Vysokotochnye televizionnye kompleksy dlya izmereniĭ bystroprotekayushchikh protsessov (High-Current Television Complexes for Measurements of Rapid Processes), Atomizdat, Moscow (1979).
[205]D. F. Barb, English translation in: Dostizheniya v tekhnike peredachi i vosproizvedeniya izobrazheniya (Progress in the Technique of Image Transmission and Reproduction), Vol. 3,

Mir, Moscow (1980), p. 180.
[206]T. L. Asatiani *et al.*, Prib. Tekh. Eksp. No. 4, 64 (1972).
[207]F. Cesaroni *et al.*, in: Proc. of the Intern. Conf. on Instrumentation for High Energy Physics, Frascati (1973), p. 241.
[208]J. Badier *et al.*, Nucl. Instrum. Methods **127**, 487 (1975).
[209]D. J. Martin, Nucl. Instrum. Methods **140**, 583 (1977).
[210]V. V. Volkov *et al.*, Prib. Tekh. Eksp. No. 3, 57 (1979).
[211]D. Holmgren, IEEE Trans. Nucl. Sci. **25**, 537 (1978).
[212]F. Villa and L. C. Wang, Nucl. Instrum. Methods **144**, 529 (1977).
[213]R. D. Fortune, CERN-ISR/DI/69-68, Geneva (1969).
[214]R. D. Fortune, CERN-ISR/DI/69-73, Geneva (1969).
[215]F. Rorbach, CERN-EF 76-1, Geneva (1976).
[216]P. Rehak and A. H. Walenta, IEEE Trans. Nucl. Sci. **27**, 54 (1980).
[217]Yu. A. Budagov *et al.*, Preprint 12-82-717 [in Russian], JINR, Dubna (1982).
[218]T. Ludlam *et al.*, Nucl. Instrum. Methods **180**, 413 (1981).
[219]W. E. Danworth and W. Ramsey, Phys. Rev. **49**, 854 (1936).
[220]F. L. Hereford, Phys. Rev. **74**, 574 (1948).
[221]M. I. Daĭon, Dokl. Akad. Nauk SSSR **64**, 305 (1949).
[222]A. I. Alikhanov and G. P. Eliseev, Zh. Eksp. Teor. Fiz. **25**, 368 (1950).
[223]G. P. Eliseev, V. A. Lyubimov, and A. M. Frolov, Dokl. Akad. Nauk SSSR **107**, 233 (1956) [Sov. Phys. Dokl. **1**, 169 (1957)].
[224]G. W. McClure, Phys. Rev. **90**, 796 (1953).
[225]F. E. Rieke and W. Prepejchal, Phys. Rev. A **6**, 1507 (1972).
[226]A. A. Tyapkin, Preprint 1-3686 [in Russian], JINR, Dubna (1968).
[227]H. Coxell and A. W. Wolfendale, Proc. Phys. Soc. **75**, 378 (1969).
[228]F. Ashton *et al.*, J. Phys. A **4**, 895 (1971).
[229]A. Buhler-Broglin *et al.*, Nuovo Cimento **45**, 520 (1966).
[230]W. Blum, K. Sochting, and U. Stierlin, Phys. Rev. A **10**, 491 (1974).
[231]V. S. Asoskov *et al.*, Preprint No. 45 [in Russian], P. N. Lebedev Physics Institute, Moscow (1975).
[232]V. S. Asoskov *et al.*, Zh. Eksp. Teor. Fiz. **76**, 1274 (1979) [Sov. Phys. JETP **49**, 646 (1979)].
[233]K. Sochting, Phys. Rev. A **20**, 1359 (1979).
[234]B. M. Golovin *et al.*, Preprint 13-81-161 [in Russian], JINR, Dubna (1981).
[235]J. L. Lloyd, Proc. Phys. Soc. **75**, 387 (1960).
[236]G. D. Alekseev *et al.*, Preprint R13-11017 [in Russian], JINR, Dubna (1977).
[237]H.-J. Gebauer, Nucl. Instrum. Methods **144**, 447 (1977).
[238]P. S. Anan'in *et al.*, Tezisy dokladov 28-go soveshchaniya po yadernoĭ spektroskopii i strukture atomnogo yadra, Alma-Ata, 1978 (Abstracts of Papers at the 28th Symposium on Nuclear Spectroscopy and Nuclear Structure, Alma-Ata, 1978), Nauka, Leningrad (1978).
[239]P. S. Anan'in, O. S. Sidulenko, and E. V. Fotin, Prib. Tekh. Eksp. No. 5, 68 (1979).
[240]P. S. Anan'in *et al.*, Pis'ma Zh. Tekh. Fiz. **5**, 106 (1979) [Sov. Tekh. Phys. Lett. **5**, 41 (1979)].
[241]P. S. Anan'in, M. N. Gushtan, and V. N. Stibunov, in: Voprosy atomnoĭ nauki i tekhniki, Seriya obshchaya i yadernaya fizika (Problems in Atomic Science and Technology, General and Nuclear Physics), No. 1 (II), Kharkov Physico-Technical Institute, USSR Academy of Sciences (1980), p. 74.
[242]P. S. Anan'in *et al.*, Avt. svid. No. 785826 ot 03.07.78 (Inventor's Certificate No. 785826 of July 3, 1978), Byull. Izobret. No. 45, 207 (1980).
[243]R. M. Sternheimer, Phys. Rev. **88**, 851 (1952).
[244]R. M. Sternheimer, Phys. Rev. **103**, 511 (1956).
[245]V. K. Ermilova *et al.*, Preprint No. 152 [in Russian], P. N. Lebedev Physics Institute, Moscow (1969).

Translated by Julian B. Barbour